Bulletin of Earthquake Engineering (2026) 24:43–92
https://doi.org/10.1007/s10518-025-02148-3

ORIGINAL ARTICLE

A new layered shell model for reinforced concrete walls I: model description and dynamic response simulations

Cem Tura[1] · **Kutay Orakcal**[1] · **M. Fethi Gullu**[2] · **Alper Ilki**[3]

Received: 28 June 2024 / Accepted: 12 March 2025 / Published online: 25 March 2025
© The Author(s) 2025

Abstract

Increasingly widespread use of nonlinear response history analysis methods for performance-based design/assessment of buildings with complex reinforced concrete (RC) wall systems has underlined the need for development and implementation of more robust nonlinear modeling approaches that can simulate important (yet commonly-ignored) nonlinear response characteristics of RC walls, such as shear-flexure-torsion interaction, plane sections not remaining plane, warping, out-of-plane behavior, nonlinear shear deformations, and shear stress migration across wall cross-section. Such advanced modeling approaches for walls need to be implemented in widely-accessible computational platforms that are capable of efficiently simulating the dynamic response of entire three-dimensional structural systems incorporating walls, under multi-directional seismic excitations. Furthermore, studies available in the literature on dynamic testing of walls and wall systems, and studies on detailed validation of refined wall models against data obtained from such dynamic test campaigns, are both scarce. With these considerations in mind, a new finite element modeling approach, referred to as the Layered Fixed-Strut-Angle Finite Element (LFSAFE) model, was developed and implemented in the widely-accessible analysis platform OpenSees. In this paper, the constitutive behavior and working principles of the LFSAFE model element are summarized. As well, nonlinear dynamic response simulation capabilities of the model are evaluated, via comparison of model response simulations with shake table test results conducted on (*i*) a half-scale isolated U-shaped wall specimen subjected to bi-directional ground accelerations, and (*ii*) a full-scale ten-story wall-frame building specimen subjected to three-directional ground accelerations. The three-dimensional dynamic response simulations presented in this paper demonstrate that the LFSAFE model is efficient in replicating, with reasonable accuracy, the experimentally-measured seismic displacement, acceleration, and deformation demands developing on both the U-shaped wall specimen and the three-dimensional wall-frame building system investigated. Capabilities of the LFSAFE model are demonstrated, and its limitations are identified.

Keywords Concrete · Wall · Model · Shell · OpenSees · U-shaped · Dynamic · Shake table

Extended author information available on the last page of the article

1 Introduction

Reinforced concrete (RC) structural walls are commonly used in building-type structures as the primary lateral-load resisting components of the structural system. They are not only effective in providing the necessary lateral stiffness for limiting the lateral displacements of the structure under wind actions or service-level earthquakes, but they are also designed and detailed to supply the structural system with sufficient lateral strength and inelastic deformation capacity (ductility) under moderate-level and severe earthquakes. With implementation of performance-based methodologies in modern seismic design codes and assessment/rehabilitation documents, together with increasingly-complex wall systems used in modern-day design and construction (e.g., core walls with complex cross-sections), robust modeling of the nonlinear seismic response of reinforced concrete structural walls has recently gained much importance among researchers. However, in typical engineering practice, fiber-based modeling approaches for walls are still commonly-used in real-life performance-based design/assessment applications worldwide. Fiber-based modeling approaches, which simulate primarily the nonlinear flexural behavior of walls (axial/flexural interaction), fail to represent important response characteristics of the wall response, including nonlinear shear/flexural/torsional interaction, nonlinear shear behavior, plane sections not remaining plane under lateral loading (shear lag), torsional warping of the cross-section, and out-of-plane behavior of wall segments. Within the framework of performance-based design and assessment, there is clearly a need for adopting improved nonlinear modeling approaches for RC walls and wall systems.

Development of robust three-dimensional modeling approaches requires experimental validation against well-documented test results on heavily-instrumented wall specimens with various response characteristics and subjected to various multi-directional loading conditions. Most of the experimental studies in recent literature on multi-directionally-loaded walls (e.g., Beyer et al. 2008a; Li and Li 2012; Constantin and Beyer 2016; Behrouzi et al. 2020; Hoult and Beyer 2021; Hoult et al. 2023a) present quasi-static test results. Accordingly, the majority of recently-developed three-dimensional wall models (e.g. Beyer et al. 2008b; Lu and Panagiotou 2014; Lu et al. 2015, 2016, 2017; Dashti et al. 2017; Feng et al. 2018; Kolozvari et al. 2018, 2019, 2021, 2022; Rojas et al. 2016, 2019; Wang et al. 2023; Ahmed et al. 2023; Hoult et al. 2023b) were experimentally-validated against quasi-static tests, during which multi-directional lateral or torsional loading was applied. Shake table tests presented in the literature on isolated wall specimens, either planar (e.g., Carillo and Alcocer, 2012, 2013; Zhang et al. 2019) or non-planar (e.g., UWS1; Almeida et al., 2024; Hoult et al., 2024), are very scarce. Comparatively, a larger number of research studies were conducted on shake table testing of wall systems or wall-frame systems, some of which are very briefly summarized herein. Panagiotou et al. (2011) presented shake table test results for a seven-story full-scale building slice tested at the University of California San Diego shake table facility. The wall-frame specimen was excited in one direction (parallel to the wall web), under four ground acceleration histories. Other researchers (Chen et al. 2016; Pantoli et al. 2016a, b) also conducted shake table tests at the UCSD facility on a five-story full-scale building slice, to correlate the seismic performance of the structural system and the non-structural components, where the specimen was tested under isolated-base and fixed-base configurations. Nagae et al. (2011, 2014) tested the E-Defense 2010 full-scale four-story wall-frame buildings with reinforced concrete and post-tensioned walls, under

scaled ground motions recorded during the 1995 Hyogoken-Nanbu earthquake, for evaluating existing design recommendations, developing new design approaches, and more accurately assessing building performance. The full-scale ten-story E-defense 2015 reinforced concrete wall-frame building was tested by Kajiwara et al. (2017), Sato et al. (2017), and Tosauchi et al. (2017), under different amplitudes of the JMA-Kobe record, under base-slip (sliding base) and fixed-base configurations. A similar E-defense test campaign was conducted in 2018, with an improved design for the beam-column connections of the ten-story building (Kang et al. 2020). The 2010, 2015, and 2018 E-defense shake table test programs were conducted under three-directional ground accelerations. He et al. (2020) performed shake table-tests on two identical nine-story wall systems, aimed to provide benchmark data to be used for improving modeling approaches. Jung et al. (2021) conducted shake table tests at the KAERI facility on a three-story wall system comprising a U-shaped wall and slabs at story levels, under varying intensities of 2016 Gyeongju earthquake ground motion record, and discussed the vibration response characteristics of the specimen, which remained mostly in the linear elastic response range during testing.

Analytical studies presented in the literature on developing advanced modeling approaches for RC walls, where the models were experimentally-validated against shake table tests on wall systems, are also scarce. Some of the relevant research efforts are summarized herein. Grange et al. (2009) presented a blind prediction of the shake table test of the seven-story building slice tested at USCD, using Timoshenko multi-fiber beam elements. Martinelli and Filippou (2009) presented blind prediction results for the same test, using the beam-column elements in OpenSees adopted for walls. Waugh and Sritharan (2010) used the same experimental campaign to validate a so-called two-dimensional centerline model, and concluded that using a two-dimensional fiber-based modeling approach was sufficient to predict the response characteristics of the walls under uni-directional dynamic loading. These studies did not address modeling of non-planar wall response and the effect of multi-directional loading on a wall system. The three-dimensional beam-truss model (Lu and Panagiotou 2014; Lu et al. 2016) was used to simulate a five-story coupled T-wall-beam-slab system tested under bi-directional ground motion (Lu and Panagiotou 2014). It was concluded that the model is effective, yet needs to be further studied in terms of simulating the dynamic response of complex structural systems under three-dimensional seismic excitations, at both global and local response levels. A quadrilateral flat nonlinear layered-shell element was developed and implemented in OpenSees (McKenna et al. 2000) by Lu et al. (2015), and the model was used to simulate the seismic response of a 142 m-high core wall–frame building designed based on the Chinese building design code, as well as a 632 m-high super-tall core wall building (Shanghai Tower), for which OpenSees documentation was also provided as a benchmark study. Later, an improved version of the model, which incorporated an updated Lagrangian formulation for geometric nonlinearity, was developed and implemented in OpenSees (Lu et al. 2017), and seismic response of the same 142 m-high core wall–frame building was simulated. In both studies, model results were validated against the nonlinear finite element analysis software MSC Marc (MSC Software 2007). Subsequently, a triangular nonlinear shell element and an explicit solution algorithm were developed and implemented in OpenSees by (Lu et al. 2019). Analysis results for the same structure, where only the coupling beams were modeled using the triangular shell element, were compared using different implicit and explicit analysis methods. The models by Lu et al. (2015, 2017, 2019) were validated against quasi-static tests conducted

on planar RC walls. However, experimental validation studies presented in these papers are limited and at the global load–displacement response level only. The models were not validated against quasi-static or shake table test results conducted on non-planar walls or wall systems subjected to multi-directional loading or excitations. However, the quadrilateral layered-shell model element by Lu et al. (2017) was later adopted by Sun et al. (2023) in simulating the response of the 2015 E-Defense 10-story wall-frame building specimen, and model results were compared with test measurements, also in terms of local (deformation) responses. Ebrahimian et al. (2018) utilized the modified compression field theory (Vecchio and Collins 1986) implemented in the finite element analysis software DIANA (TNO DIANA BV 2011), for simulating the fixed-base five-story full-scale building slice tested at UCSD by Chen et al. (2016); Pantoli et al. (2016a, b). Eight-node Mindlin-Reissner quadrilateral serendipity shell elements were used for the slabs and shear walls, and uncertainties in the simulations stemming from the constitutive parameters of the material model were identified. Rahman et al. (2022) simulated the three-story wall structure tested at the KAERI (Jung et al. 2021), using layered-shell, fiber beam-column, and beam-truss elements available in OpenSees, for identifying the most consistent approach for nonlinear analysis of wall systems under dynamic loading, although they were unable to identify an optimum modeling methodology. Xiao et al. (2024) investigated the influence of different modeling assumptions in ABAQUS (Smith 2014) on response simulation of three-story wall structure tested by Jung et al. (2021), where the concrete elastic modulus and foundation flexibility were the primary parameters of investigation. They also emphasized the importance of system identification and model updating towards improving the accuracy of analysis results. More recently, Isaković et al. (2023) co-edited a special issue on simulation of the 2015 and 2018 E-defense full-scale ten-story wall-frame buildings with sliding-base and fixed-base configurations. In this special issue, various response simulation studies were published, where different analytical modeling approaches for walls (both macroscopic and finite element) were utilized. Most recently, Ghosh et al. (2024) simulated the 2010 E-defense four-story wall-frame building shake table tests, using the previously-validated (e.g., Dashti et al. 2017) curved shell element in DIANA (2022) for the walls and slabs, compared model results with test measurements at both global and local (deformation) response levels, and suggested further experimental validation of the model against additional shake table tests.

Robust finite element wall models that are available in commercial analysis software (e.g., DIANA (2024), LS-DYNA (ANSYS Inc 2024), ADINA (2024), etc.) have recently been finding their way into real-life design applications. However, problems related to modeling of entire structural systems and the lack of flexibility in calibration or updating of the material constitutive models, apply to most of the readily-available finite element wall models. As well, convergence rates and run times of such generally impair their use in three-dimensional analysis of large and complex structural systems, as required in real-life performance-based seismic design applications. On the other hand, use of research-oriented finite element wall models is generally restricted to a narrow research community mostly involved in their development, whereas models that are accessible by all, through research-oriented computational platforms (e.g., OpenSees, McKenna et al. 2000), are extremely few (e.g., Lu et al. 2015, 2017, 2019).

Given these shortcomings, this study aims to contribute to the existing level of knowledge and capabilities on three-dimensional modeling and nonlinear seismic response simulation of walls or wall systems, by presenting a new layered-shell model element for RC

walls, which was developed and implemented by the authors in OpenSees (McKenna et al. 2000). The model is referred to as the Layered Fixed-Strut-Angle Finite Element (LFSAFE) model. This paper provides a description of the constitutive behavior and working principles of the model, and also presents nonlinear dynamic response simulations obtained using the model for: (*i*) a bi-directional shake table test conducted very recently on a U-shaped wall specimen (UWS1; Almeida et al., 2024; Hoult et al., 2024) and, (*ii*) the 2015 E-Defense three-directional shake table tests conducted on a full-scale ten-story wall/frame building specimen (Kajiwara et al. 2017; Sato et al. 2017; Tosauchi et al. 2017). The present paper does not aim to provide a detailed evaluation of the accuracy of the LFSAFE model in predicting shake table test results, since other factors (e.g., assumed damping) are also expected to influence the accuracy of the analysis results. Rather, the objective of the present paper is to demonstrate the overall nonlinear dynamic response simulation capabilities of the LFSAFE model, for both isolated walls and wall/frame systems, under multi-directional seismic excitations. Detailed experimental validation of the LFSAFE model is presented in a companion paper (Tura et al. 2025), where quasi-static response predictions of the model are compared, at both global (e.g., load–displacement, torque–twist) and local (deformation, strain) response levels, with results of carefully-controlled quasi-static tests on heavily-instrumented non-planar (U-shaped and H-shaped) wall specimens subjected to various multi-directional (uni-directional lateral, bi-directional lateral, torsional, combined lateral and torsional) loading conditions.

2 The Layered Fixed-Strut-Angle Finite Element (LFSAFE) model

The Layered Fixed-Strut-Angle Finite Element (LFSAFE) model is an improved and extended version of the so-called Fixed-Strut-Angle Finite Element (FSAFE) model (Gullu and Orakcal 2021). The 4-node 8-degrees-of-freedom formulation of the original FSAFE model element (with 2 translational DOFs at each node), was incapable of simulating the out-of-plane behavior of a rectangular wall or wall segment (web or flange) in a non-planar wall, since its single-layer (membrane) formulation did not incorporate out-of-plane displacements or rotations. Furthermore, the original FSAFE model element did not include any drilling (in-plane rotational) degrees of freedom, and incorporated a single Gauss integration point in its formulation. Nevertheless, accuracy of the FSAFE model has been extensively validated against test results for relatively-slender, medium-rise, and low-rise planar walls subjected uni-directional lateral loading (Gullu et al., 2019; Gullu and Orakcal 2021), as well as U-shaped walls tested under bi-directional lateral loading (Bilgin et al. 2021; Kolozvari et al. 2022). The extensions (as well as improvements) implemented on the baseline FSAFE model formulation, for developing the LFSAFE model element presented in this paper, includes: (*i*) formulation of a new three-dimensional model element with 4 nodes and 6 DOFs (3 translational and 3 rotational) at each node, (*ii*) implementation of a multi-layered shell formulation (with multiple membranes comprising the shell element) for simulating nonlinear out-of-plane flexure, (*iii*) inclusion of drilling (in-plane rotational) degrees of freedom, which allow direct connectivity between wall element nodes and frame elements, rather than using "embedded beams" (e.g., Perform3D; Computers and Structures Inc., 2023), (*iv*) improvement of the constitutive model for reinforcing steel to represent

reinforcement buckling behavior, (*v*) implementation of the model element in the open-source computational platform OpenSees (McKenna et al. 2000).

The model's three dimensional and 24-DOF formulation allows direct implementation in three-dimensional models of entire structural systems. In-plane strains on the LFSAFE model element are calculated using 3rd -order Hermite shape functions adopted for displacement interpolation, and the corresponding tangent stiffness matrix and restoring force vector are obtained via 3×3 Gauss integration. Out-of-plane kinematics of the model element is defined based on the Discrete Kirchhoff Quadrilateral Plate element formulation (Batoz and Tahar 1982). Nonlinear model element behavior corresponding to both the in-plane and out-of-plane deformation modes are obtained from the in-plane (plane-stress) behavior of the reinforced concrete layers (membranes) comprising the shell element. Out-of-plane shear behavior of the thin-shell-type LFSAFE model element is assumed linear elastic. Details on the constitutive behavior and the mechanical working principles of the LFSAFE model are described in the following subsections.

2.1 The constitutive Fixed-Strut-Angle Model (FSAM) for RC membrane behavior

The LFSAFE model element incorporates the so-called Fixed-Strut-Angle Model (FSAM, Orakcal et al. 2019) as the constitutive plane-stress RC panel (membrane) model for defining the membrane behavior of each layer in the LFSAFE model element. The FSAM was developed and validated based on test results presented in the literature for RC panel (membrane) specimens tested under various stress states and strain histories. Formulation of the constitutive model FSAM (Fig. 1a), follows an average strain, smeared stress, and fixed-crack-direction approach, with perfect bond assumed between concrete and reinforcing steel bars. Bond slip deformations are neglected in the formulation of the FSAM, which renders it incapable of simulating possible bond slip failures in a wall (e.g., along deficient lap splices), or capturing strain/yield penetration effects associated with bar extension/slip

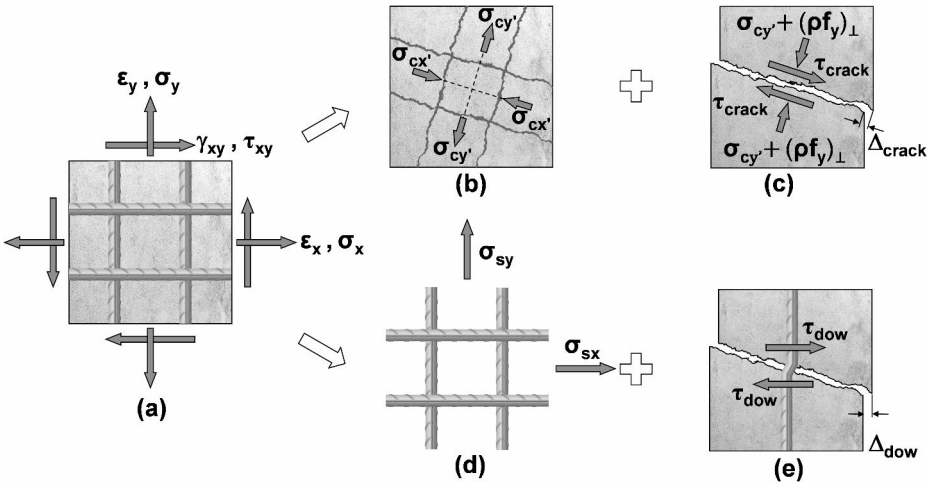

Fig. 1 Constitutive Fixed-Strut-Angle Model (FSAM): (**a**) strain field and corresponding stress field on a RC membrane, (**b**) concrete stresses along fixed struts, (**c**) shear aggregate interlock stresses along cracks, (**d**) uniaxial stresses in reinforcement, (**e**) dowel stresses in reinforcement. (modified from Gullu et al., 2019)

deformations developing within the foundation of a wall and accumulating at the wall-foundation interface.

In this constitutive model, reinforced concrete behavior is simulated using primarily uniaxial stress–strain relationships for concrete struts along two fixed strut (crack) directions (Fig. 1b), and for reinforcing steel in the two orthogonal reinforcement directions (Fig. 1d). The model formulation also incorporates mechanically-defined hysteretic response characteristics for the shear aggregate interlock effects along crack surfaces (Fig. 1c), as well as dowel action on both vertical and horizontal reinforcement (Fig. 1e). The resultant average (smeared) stress field developing on the panel element corresponding to the applied strain field, is obtained via superposition of uniaxial concrete stresses developing along the two fixed strut directions, with shear stresses developing along crack surfaces and smeared uniaxial and dowel stresses developing in the horizontal and vertical reinforcement (Fig. 1a).

2.2 Cracking and fixed-strut behavior of concrete in the FSAM

In the FSAM formulation, during the uncracked stage of concrete behavior, the principal stresses in concrete are obtained in the principal strain directions (Fig. 2a), assuming principal strain and stress directions in concrete coincide until first cracking. This approach is

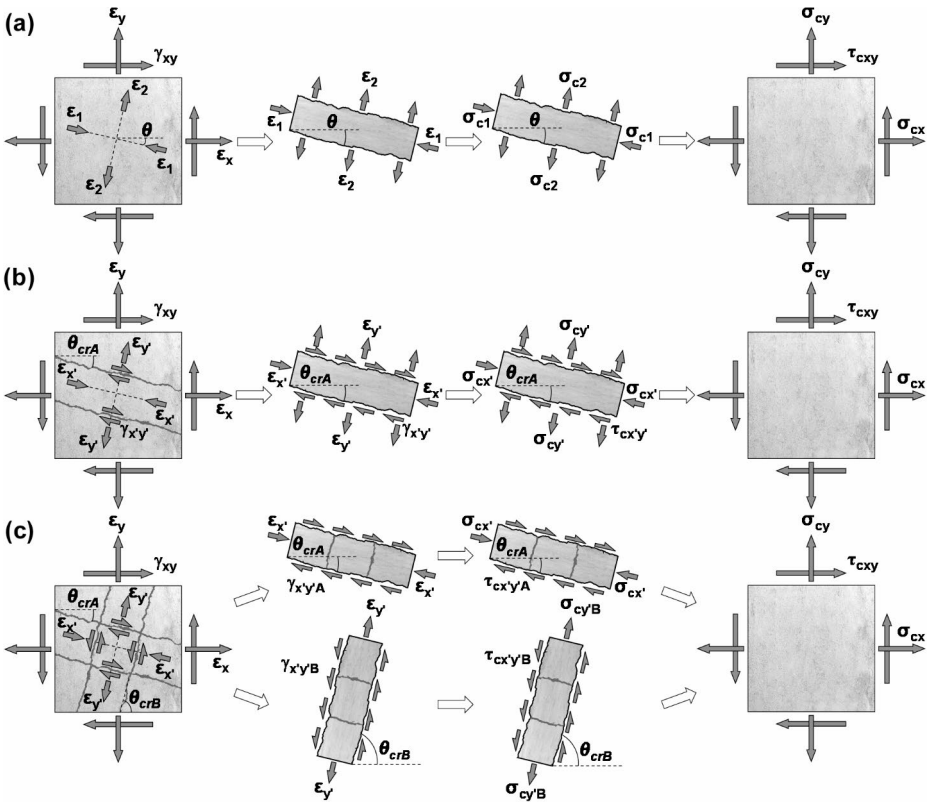

Fig. 2 FSAM concrete behavior: (**a**) uncracked, (**b**) after formation of the first crack, (**c**) after formation of the second crack (modified from Gullu et al., 2019)

similar to rotating-angle constitutive modeling approaches presented in the literature (e.g., Modified Compression Field Theory, Vecchio and Collins 1986). Subsequently, when the principal tensile strain on the membrane first exceeds the cracking strain of concrete (ε_t in Fig. 3a), the first crack develops, forming the first "fixed strut" parallel to the cracking angle, perpendicular to the principal strain direction (θ_{crA} in Fig. 2b). After formation of the first crack, a fundamentally uniaxial stress–strain behavior (that also considers biaxial softening effects) is assumed for concrete, in parallel and perpendicular directions to the first crack (first strut), while the principal strain directions in concrete continue to rotate depending on the imposed strain fields. At this stage, shear stresses also develop along the crack surface, due to the constitutive mechanisms defined for shear stress transfer across the cracks, as described in a later section. During subsequent loading, upon load reversal, the second crack (strut) is assumed to form in perpendicular direction to the first crack (i.e., the FSAM assumes orthogonal cracks), when the strain along the first strut exceeds the concrete cracking strain upon unloading from compression ($\varepsilon_0+\varepsilon_t$ in Fig. 3b). During further loading/unloading, principal strain directions continue to rotate based on the applied strain field, whereas uniaxial stresses are assumed to develop in concrete, along the two fixed strut (crack) directions (Fig. 2c). The two concrete struts undergo interchanging axial tension and compression, and concrete behavior along these fixed struts (θ_{crA} and θ_{crB} in Fig. 2c) are represented using the uniaxial hysteretic concrete stress-strain relationship, also modified to consider biaxial softening effects. During this stage, shear stresses developing along crack surfaces, resulting from the stress transfer mechanisms adopted along the cracks, is also considered in calculation of the resultant stress field on concrete. The shear stresses developing on the crack surfaces cause the principal stress directions in concrete to deviate from the fixed strut (crack) directions. In summary, the FSAM generates the resultant stress field on cracked concrete as the superposition of two components: (*i*) the uniaxial stresses developing in concrete along the fixed strut directions, and (*ii*) the shear (interlock) stresses developing along crack surfaces. Considering the total (resultant) stress field on concrete, the principal stress planes therefore deviate from the fixed crack planes. Details on the working principles of the FSAM, as well as its experimental validation against cyclic RC panel (membrane) tests presented in the literature (Stevens et al. 1991; Mansour and Hsu 2005), are available in the publications by Orakcal et al. (2019), Bekaroglu (2019), and Ulugtekin (2010).

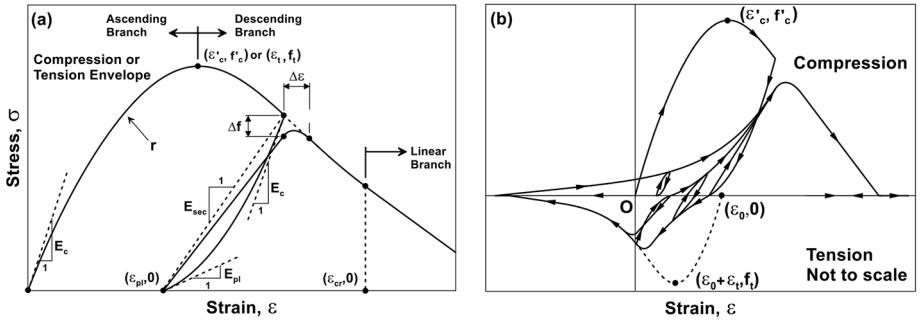

Fig. 3 Chang and Mander (1994) uniaxial constitutive model for concrete: (**a**) Compression or tension envelope, and (**b**) hysteretic rules

2.3 Material constitutive models

In the constitutive FSAM formulation of the present LFSAFE model element, the uniaxial hysteretic behavior of concrete along the two fixed struts is represented using the refined constitutive relationship by Chang and Mander (1994). (Fig. 3). The adopted concrete model reflects detailed hysteretic behavioral characteristics of concrete, such as continuous hysteretic behavior (with slope continuity) under compression and tension, progressive stiffness degradation, gradual gap closure, and tension stiffening. Although the concrete stress–strain relationship is fundamentally uniaxial, biaxial softening effects on concrete, including compression softening (Vecchio and Collins 1993) and hysteretic biaxial damage (Mansour et al. 2002), are also incorporated in the concrete stress–strain behavior adopted in FSAM along the two strut directions. As well, the monotonic tension envelope of the model is calibrated to represent the effect of tension stiffening on the average stress–strain behavior of concrete after cracking, according to the relationship proposed by Belarbi and Hsu (1994). For considering the effect of confinement on the stress–strain behavior of concrete in compression, the LFSAFE model element uses a uniaxial constitutive model (Mander et al. 1988), for which the confined stresses and strains are considered in perpendicular direction to transverse reinforcement. This is a simplification in the model element formulation, as the compression struts developing in the model elements will not necessarily be vertically-oriented. However, for slender or moderate-aspect-ratio walls with flexure-dominated coupled shear-flexural responses, in the model elements representing the wall boundary regions where confinement is provided, crack orientations predicted by the model are typically very close to horizontal (corresponding to approximately vertical compression struts), which makes this simplification a reasonable one.

To describe the uniaxial stress–strain behavior of the horizontal and vertical reinforcing steel bars in the web region of a wall, as well as the horizontal bars in the wall boundary regions, the well-known uniaxial hysteretic constitutive model developed by Menegotto and Pinto (1973) (extended by Filippou et al. (1983) to incorporate strain hardening effects) (Fig. 4a), is adopted. For the longitudinal reinforcement located in wall boundary regions, in order to represent reinforcing bar buckling behavior, the hysteretic constitutive relationship proposed by Dhakal and Maekawa (2002a) is adopted in the present model formulation, together with a simplification of the hysteretic rules that neglects the linear transition regions between the hysteretic loops and the monotonic compression and tension envelopes (Fig. 4b). In this constitutive model, the monotonic compression envelope that considers

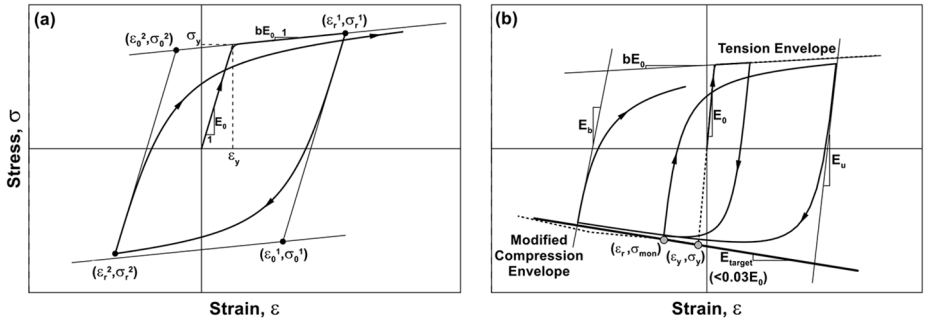

Fig. 4 Reinforcing steel constitutive models: (**a**) Menegotto and Pinto (1973) (**b**) simplified Dhakal and Maekawa (2002a)

reinforcement buckling behavior, is first constructed. In construction of the modified compression envelope, buckling of the reinforcing steel bar is associated with the product of the slenderness ratio and the square root of the reinforcement yield strength ($L/D\sqrt{f_y}$), as well as post-yield characteristics of the tension envelope. The slenderness ratio corresponding to the controlling buckling mode is determined using the procedure by Dhakal and Maekawa (2002b), also considering in-plane and out-of-plane buckling modes across multiple tie spacings. The hysteretic formulation of the model is based on the Menegotto and Pinto (1973) formulation, with strain-history-based yield asymptotes (with negative slope) defined in compression. The slope of the compression yield asymptote (E_{target} in Fig. 4b) is defined as equal to slope of the line connecting the yield point under compression (ε_y, σ_y in Fig. 4b) with the compressive stress on the modified compression envelope (ε_r, σ_{mon} in Fig. 4b) corresponding to the maximum compressive strain experienced during the previous strain history. However, E_{target} should not exceed a maximum value of $0.03E_0$. Furthermore, unloading stiffness values from tension (E_u in Fig. 4b) and compression (E_b in Fig. 4b) are defined based on the empirical equations provided by Dhakal and Maekawa (2002a). In both of the hysteretic constitutive models adopted for reinforcing steel (with and without buckling), Bauschinger's effect is represented through the cyclic stiffness degradation parameters (R_0, a_1, and a_2) embedded in their formulation. Furthermore, in both constitutive models, tension stiffening effects on the longitudinal reinforcing bars are represented using the relationships proposed by Belarbi and Hsu (1994) for modifying the tensile yield strength and tensile strain hardening ratio of bars embedded in concrete. In the present model formulation, the constitutive relationships adopted for reinforcing steel do not incorporate reinforcement rupture, post-buckling rupture (buckling-fatigue behavior), or low-cycle fatigue effects, which is a significant limitation. However, these effects can be incorporated in the model formulation directly at the material model level, independently from the model element formulation.

2.4 Shear transfer mechanisms across cracks

In the constitutive FSAM formulation, for representing shear stress transfer across the fixed cracks, shear stresses developing along the crack surfaces are calculated using a physical friction-based constitutive relationship, and are then superimposed with the concrete stresses along the struts in order to obtain total stress field in concrete. The friction-based constitutive relationship representing shear aggregate interlock along crack surfaces relates the maximum shear stress developing along a crack surface to the compressive stress in concrete strut ($\sigma_{c\perp}$ in Fig. 5a, which is equal to $\sigma_{cy'}$ in Fig. 1c) in perpendicular direction to the crack, through a friction coefficient (η in Fig. 5a). A smeared "clamping stress" created by the perpendicular component of the yield strength of the reinforcement straddling the crack (i.e., $(\rho f_y)\perp$ in Figs. 1c and 5a), is also considered in the compressive stress to be multiplied with this friction coefficient. Therefore, the two components of normal stress acting on a crack surface are: (*i*) varying compressive stresses in concrete perpendicular to the crack direction, and (*ii*) a constant clamping stress created by the reinforcement. When the concrete stress perpendicular to the crack direction is zero or a tensile stress (due to tension stiffening); i.e., when the crack is open, contribution of the first component to shear aggregate interlock reduces to zero. In order to describe this friction-based constitutive relationship, the monotonic envelope and the hysteresis rules proposed by Tassios and Vintzēleou (1987) for rough crack surfaces (along which clamping is observed), is adopted (Fig. 5a).

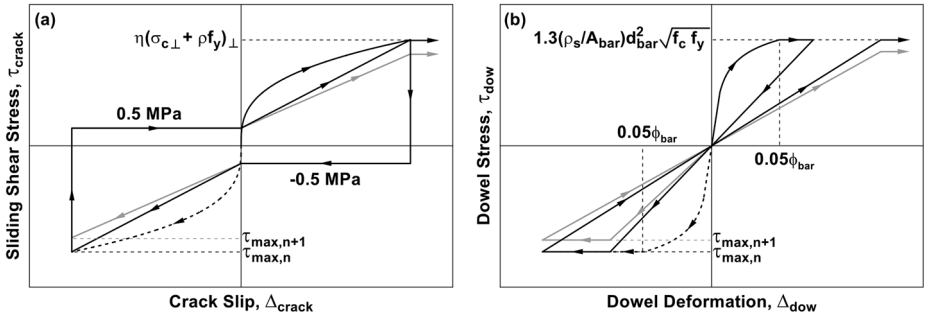

Fig. 5 Constitutive models for shear stress transfer mechanisms across cracks: (**a**) shear aggregate interlock along crack surfaces, (**b**) dowel action on reinforcement

Assuming a constant clamping stress along a crack surface, irrespective of the crack width, is a simplified approach adopted in the constitutive membrane model (FSAM) formulation. However, experimental validation studies that were conducted previously using a simpler and single-layered (membrane) formulation of the LFSAFE model, against planar walls tested under in-plane loading (FSAFE model– Gullu and Orakcal 2021; Gullu et al., 2019; Gullu et al. 2018a, b; Gullu 2019), have revealed that even with this simple approach, the model provides accurate response predictions for slender walls with flexure-dominated responses, as well as moderate-aspect-ratio walls with shear-flexure interaction behavior and low-rise walls with shear-controlled responses. In these studies, it was observed that for walls with predominantly flexural or coupled shear/flexural responses, consideration of the clamping component of shear aggregate interlock mechanism is not significantly influential on the model results. For such walls, the boundary region under flexural compression is where the majority of the internal shear stresses on crack surfaces develop, primarily due to the normal stress component of the shear aggregate interlock mechanism (i.e., due to the compressive stress developing in concrete in perpendicular direction to the crack). Consideration of the clamping mechanism becomes more influential (at least noticeably) on the model response predictions for low-rise walls with shear-controlled responses (Gullu et al. 2018a, b; Gullu 2019), and the constant clamping stress assumption adopted in the FSAM formulation was found to be adequate for obtaining reasonably accurate response predictions for such walls also. Furthermore, it is acknowledged that the friction coefficient (η in Fig. 5a), which is used to define the shear aggregate interlock mechanism along crack surfaces, must inherently depend on the concrete aggregate size. However, to the authors' knowledge, comprehensive test data that relates the shear aggregate interlock behavior of cracked interfaces to aggregate size, is not available at present. Therefore, the shear aggregate interlock friction coefficient has to be defined in a somewhat ad-hoc manner, independently of the mean aggregate size. Previous studies conducted using the single-layer version of the LFSAFE model (Gullu and Orakcal 2021; Gullu et al., 2019; Gullu et al. 2018a, b; Gullu 2019) have revealed that using a friction coefficient in the range of 0.3 to 0.5 is suitable for modeling of one-third and half-scale wall specimens, and provides reasonable model predictions for walls with shear-dominated responses, as well as for walls with flexure dominated responses and shear-flexure interaction behavior. In the present paper, and in the companion paper also (Tura et al. 2025), a friction coefficient of 0.4 is adopted for modeling of all of the test specimens investigated, similarly to the coefficient of 0.44

recommended by Tassios and Vintzēleou (1987) for rough crack surfaces, based on results of cracked interface tests.

The constitutive membrane model FSAM relates the slip deformation along the crack interface to the shear stress transferred, where the slip deformation (Δ_{crack} in Fig. 1c) along the crack surface is calculated by multiplying the shear strain in the crack direction with the nominal crack spacing defined by Vecchio and Collins (1986) and Vecchio (2000). The nominal crack spacing is correlated with the spacing of horizontal and vertical reinforcing bars, as well as the crack angle. In the model element, for the cover concrete and core concrete layers that do not incorporate reinforcement, crack spacing is assumed to be identical to that calculated for the layers that include reinforcement. This is believed to be a reasonable assumption, as it is commonly observed in real-life RC structures. It must be mentioned that definition of crack spacing in the model formulation is required only for relating the shear strains developing in crack directions (at the Gauss integration points of the model element), to crack slip (sliding) deformations developing along crack surfaces, and therefore relates only to the tangent stiffness characteristics of shear aggregate interlock constitutive relationship applied along the crack surfaces.

Contribution of dowel action on both the horizontal and vertical reinforcing bars on the shear stress field developing on the panel element is also incorporated in the FSAM model formulation, via adopting the dowel force vs. deformation monotonic envelope and the hysteresis rules defined by Vintzēleou and Tassios (1986, 1987) (1987). In this study, these hysteresis rules were simplified into origin-oriented hysteresis rules (Fig. 5b). To correlate dowel forces and deformations with dowel stresses and strains, the smeared-stress-strain constitutive modeling approach proposed by He and Kwan (2001) is used. In this approach, the dowel deformation (Δ_{dow} in Figs. 1e and 5b) on the reinforcing steel bars is correlated with shear and tensile strains across the crack, as well as an effective dowel length, where the dowel length is determined using a beam (reinforcing bar) on a semi-elastic foundation (concrete) analogy. Smeared dowel stresses perpendicular to the direction of the reinforcing bars are obtained from the corresponding dowel forces. The reinforcing steel stresses are then superimposed with the smeared dowel stresses, and then back-converted to tensile and shear stresses along the crack surface. Lastly, in both of the constitutive models adopted for shear aggregate interlock and dowel action, cyclic degradation effects on the interlock and dowel stresses are also considered, using the history-dependent cumulative-deformation-based empirical relationships first proposed by Tassios and Vintzēleou (1987) and Vintzēleou and Tassios (1986, 1987), later modified by Thermou et al. (2014).

2.5 The LFSAFE model element

The LFSAFE (Fig. 6) model element implemented in this study in OpenSees, with its six (three translational and three rotational) degrees of freedom (DOF) at each node, builds upon the baseline formulation of the currently-available Discrete Kirchhoff Generalized Quadrilateral shell element (ShellDKGQ), which was previously implemented in OpenSees by Lu et al. (2017). The ShellDKGQ element combines the membrane element GQ12 (Xu and Long 1993) with the well-known plate bending element DKQ (Batoz and Tahar 1982), in order to generate a complete 24-DOF shell element formulation.

The membrane formulation of the ShellDKGQ element utilizes bi-linear and linear-quadratic shape functions for the description of displacement fields associated with translational

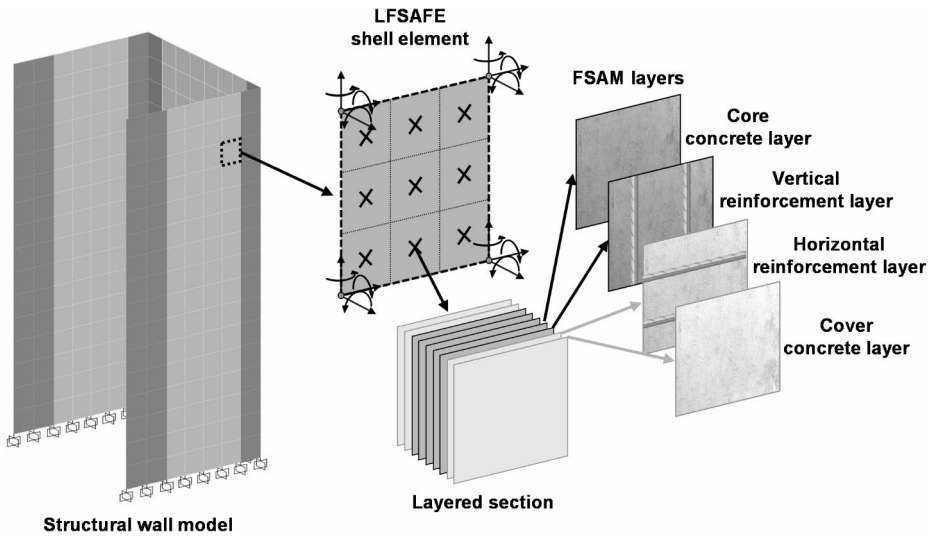

Fig. 6 Layered Fixed-Strut-Angle Finite Element (LFSAFE) model element

DOFs and rotational (drilling) DOFs, respectively. However, drilling rotations obtained using the ShellDKGQ element were found geometrically-incompatible with translational displacements at the nodes of the shell elements, in cases where moment transfer is required at the drilling DOFs of the element. The strain interpolation functions adopted in the ShellDKGQ element for the drilling degrees of freedom provide insufficient drilling stiffness, resulting in excessive in-plane (drilling) rotations at the shell element nodes, when frame elements are connected to the shell elements in their plane. Furthermore, rotations obtained along the drilling DOFs at the other nodes of the wall model (to which the line elements are not connected) are not geometrically-compatible with the translational nodal displacements, and those nodes also undergo excessive drilling rotation together with the node to which the line element is connected. Same results are obtained when either 2×2 or 3×3 Gauss integration is used in the GQ12 model element formulation.

In order to remedy this connectivity problem between the nodes of the ShellDKGQ element and connecting frame elements, the membrane formulation of the original ShellDKGQ element was modified. In LFSAFE model element formulation, bi-linear and linear-quadratic shape functions (that were originally used in definition of displacement interpolation functions of the GQ12 element) are replaced with linear-cubic interpolation functions derived using third-order Hermite shape functions for both the translational DOFs and rotational DOFs, and 3×3 Gauss integration is used for generation of the stiffness matrix and the resisting force vector, similarly to the approach adopted and described in detail by Rojas et al. (2016). When this formulation is adopted, the LFSAFE model element provides drilling rotations that are kinematically-compatible with the translational displacements at the model element nodes, and also generates sufficient drilling stiffness at the element nodes so that more physical moment transfer is attained between the wall model and connecting frame elements (instead of excessive drilling rotations developing at wall and frame element connections).

To illustrate, deformed shapes obtained using analysis models generated in OpenSees for two slender walls connected together by beam (line) elements (e.g., coupled wall systems), where either ShellDKGQ or LFSAFE elements are used for modeling of the walls and linear elastic line (frame) elements with plastic flexural hinges at the ends are used for modeling of the beams, are compared in Fig. 7. In the figure, rotations at drilling degrees of freedom of the wall model are shown with the cross symbols plotted in red. As can be observed in Fig. 7a, when ShellDKGQ elements are used for modeling of the walls, excessive drilling rotations develop not only at the nodes where the beams are connected, but also at other nodes of the wall model. Furthermore, plastic rotations do not develop on the beams, indicating that bending moments transferred to the beams are relatively low, since the wall model nodes to which the beams are connected undergo excessive drilling rotations. When the walls are modeled using LFSAFE elements (Fig. 7b), the beams reach their moment capacities and undergo plastic rotations, due to the sufficient drilling stiffness of the wall model nodes to which the beams are connected, and more kinematically-compatible drilling rotations develop on all other nodes of the wall model.

Accurate definition of drilling stiffness in membrane or shell elements is a challenging task that is subject much uncertainty, since application of a concentrated moment on a single dimensionless node is not entirely physical, and the problem is very much subject to localization effects (i.e., model element discretization and/or nonlinear strain localization). For reinforced concrete walls, moment transfer from a connecting beam or a coupling beam is not physically in the form of a concentrated moment, and the drilling stiffness of the region to which the beam is connected will also depend on the reinforcement in the region, which consists of not only the wall reinforcement, but also the beam reinforcement extending into the region. However, as illustrated in Fig. 7, the LFSAFE model element is clearly more physical compared to the ShellDKGQ element (or the GQ12 membrane element), in terms of drilling stiffness characteristics and kinematic compatibility between drilling and translational DOFs. In this respect, the LFSAFE shell element introduced in this study, as well as the QLMEDD membrane element and the QTFLS shell element developed by Rojas et al. (2016, 2019), are improvements towards more physical connectivity between wall model elements and line (beam) elements.

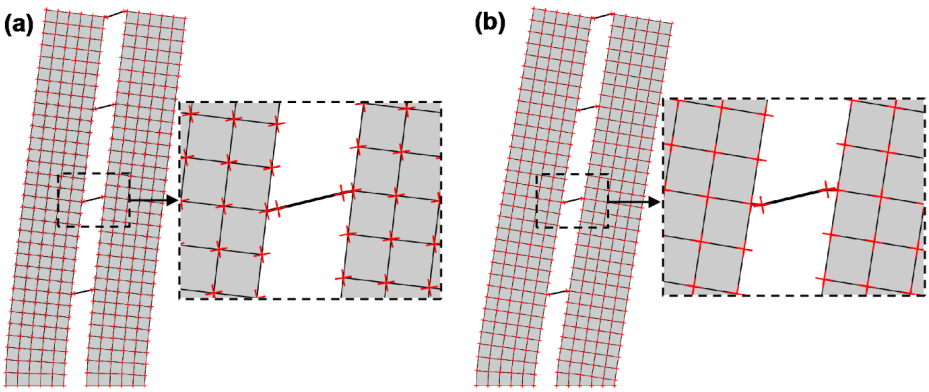

Fig. 7 Analytical deformed shapes obtained for a coupled wall system using: (**a**) ShellDKGQ model elements (with bi-linear and linear-quadratic shape functions and 2 × 2 Gauss integration), (**b**) LFSAFE model elements (with Hermite shape functions and 3 × 3 Gauss integration)

The out-of-plane behavior of the LFSAFE model element is formulated by adopting the Discrete Kirchhoff Quadrilateral (DKQ, Batoz and Tahar 1982) plate element formulation of the ShellDKGQ element, where through-thickness shear strains due to out-of-plane translational DOFs are neglected, and only curvatures due to out-of-plane rotations are considered. However, since the nonlinear out-of-plane behavior of the shell element is defined using a layered section formulation, where membrane strains are extrapolated using a combination of membrane and plate deformation modes, curvatures due to out-of-plane bending of the plate element are also extrapolated at nine Gauss points, differently from than the original ShellDKGQ element with four Gauss points. Further information about the DKQ plate element formulation can be found in Batoz and Tahar (1982).

The LFSAFE model element employs the currently-available layered section formulation (Lu et al. 2015) in OpenSees, where in-plane and out-of-plane nonlinear behavior are coupled. In the out-of-plane direction of the model element, the plane-sections-remain-plane kinematic assumption is employed for obtaining the in-plane strains developing in each membrane layer. The in-plane strains (ε_x, ε_y, γ_{xy}) at each Gauss point of each membrane layer are obtained by first calculating the element centerline (mid-thickness) strains associated with the in-plane DOFs, and then adding to these, the in-plane strains developing in each layer due to out-of-plane curvatures at the Gauss points. This results in a linear strain distribution (constant curvature) across the thickness (among the layers) of the model element. This linear strain distribution applies to the vertical, horizontal, and shear strains on the membrane layers, based on the strains calculated (using the in-plane displacement field) at the model element mid-thickness, and the out-of-plane rotation field. Derivation of the displacement fields and the strain fields in each membrane layer, from the in-plane displacement and the out-of-plane rotation fields of the model element, are provided in Eqs. 1, 2, and 3. In the equations, notations u and v correspond to the displacement fields associated with the in-plane DOFs, u_{layer} and v_{layer} represent the total displacement fields including contribution of out-of-plane curvatures, θ_x and θ_y correspond to out-of-plane rotation fields about the local x and y axes of the model element, and z_{layer} denotes the distance between a specific membrane layer to the centerline of the element thickness.

$$u_{layer} = u + z_{layer}\theta_y \tag{1}$$

$$v_{layer} = v - z_{layer}\theta_x \tag{2}$$

$$\begin{bmatrix} \varepsilon_x \\ \varepsilon_y \\ \gamma_{xy} \end{bmatrix} = \underbrace{\begin{bmatrix} \partial u/\partial x \\ \partial v/\partial y \\ \partial u/\partial y + \partial v/\partial x \end{bmatrix}}_{\text{From in - plane displacement fields}} + z \underbrace{\begin{bmatrix} \partial \theta_y/\partial x \\ -\partial \theta_x/\partial y \\ \partial \theta_y/\partial y - \partial \theta_x/\partial x \end{bmatrix}}_{\text{From out - of - plane rotation fields}} \tag{3}$$

The stress states and the material tangent stiffnesses corresponding to the membrane strain fields attained from layered section formulation are obtained from the constitutive RC membrane model FSAM for each layer, and are used in generation of the element resisting force vector and the element tangent stiffness matrix. Due to the layered formulation of the model element, strain predictions are obtained not only at the centerline (mid-thickness) of the element, but also at the edges of the wall cross-section. The significance of this feature becomes evident when the maximum (e.g., outer-surface) compressive strains are being predicted

on the web, flanges, or web-flange intersections of a non-rectangular wall cross-section, especially when the location of the neutral axis falls within the thickness of a wall segment. As well, the layered formulation of the model element permits more detailed cross-section definitions, with consideration of different confinement characteristics for concrete along the wall thickness (unconfined cover vs. confined core layers), as well as, defining the precise locations of the reinforcement layers, as representatively shown in Fig. 8. For example, in a single model element, an unconfined stress–strain relationship can be adopted for the cover concrete layers, while a confined stress–strain relationship can be used for the core (confined) concrete layers. During the analysis, the unconfined cover concrete layers will be subjected to earlier and much more pronounced compressive stress degradation (along the descending region of the stress–strain relationship), compared to the confined concrete layers, even under equal compressive strain demands. Furthermore, the nonlinear flexural behavior of the model element in the wall out-of-plane direction allows simulating asymmetrical concrete crushing or asymmetrical reinforcement yielding across the thickness of a wall segment. It must be noted that the robustness of the out-of-plane formulation of the LFSAFE model element was validated upon comparison of analysis results obtained under loading in the out-of-plane direction of the model element, against experimental data from cyclic loading tests conducted on reinforced concrete components with predominant nonlinear flexural behavior. For example, although not shown here for brevity, for the rectangular

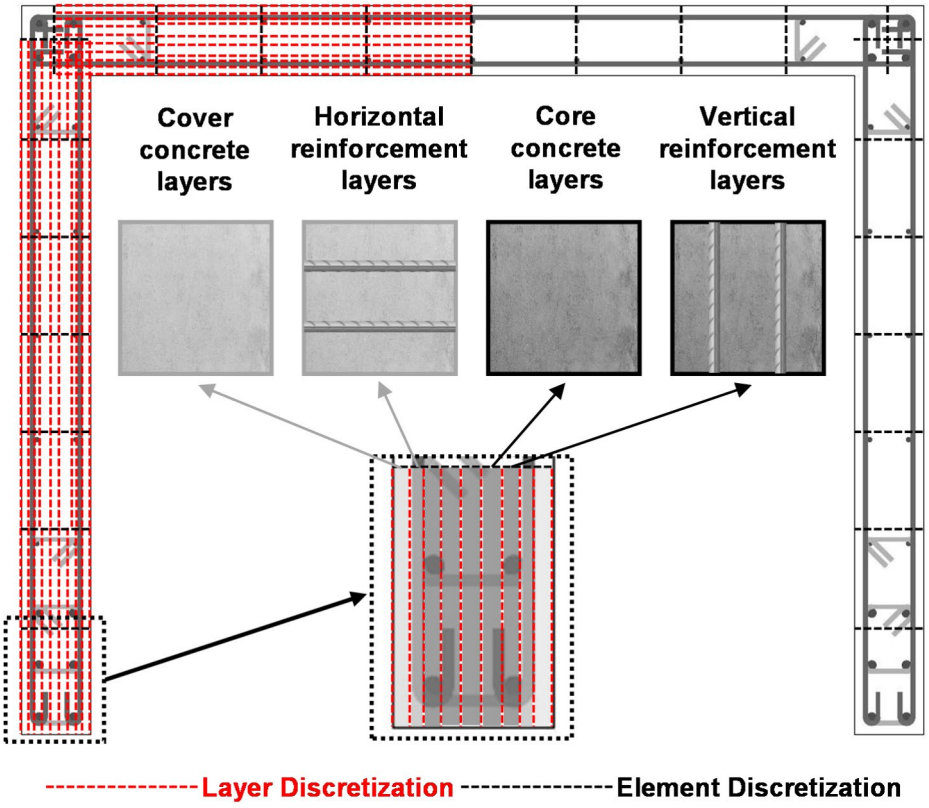

Fig. 8 Model element and layer discretization for a representative U-shaped wall cross-section

wall specimen RW2 (Thomsen and Wallace 2004), using a single LFSAFE model element to describe the entire wall cross-section (with the cross-section discretized into layers of the model element in its out-of-plane direction) was found to accurately capture the predominantly flexural response of the wall specimen, with the same level of accuracy that would be expected from a fiber-based model.

3 Shake table test programs

In order to demonstrate the dynamic response simulation capabilities of the LFSAFE model, the two shake table test programs conducted by Hoult et al. (2024) and Kajiwara et al. (2021) are simulated in OpenSees. The first test specimen is a half-scale isolated U-shaped wall specimen (UWS1, Almeida et al. 2024; Hoult et al. 2024) tested very recently under consecutive uni-directional and bi-directional ground excitations, at the National Laboratory for Civil Engineering (LNEC), Portugal. The second test specimen is a full-scale ten-story wall-frame building structure (Kajiwara et al. 2017; Sato et al. 2017; Tosauchi et al. 2017) tested in 2015 at the E-Defense shake table facility in Japan, under three-directional excitation that also includes the vertical ground motion component.

The U-shaped wall specimen UWS1 (Fig. 9b), has the same cross-sectional dimensions and reinforcement detailing with specimens UW1 and UW2, which were previously tested by Hoult et al. (2023a) under quasi-static loading. Detailed experimental validation of the LFSAFE model against those tests, as well as other non-planar walls, are presented in the companion paper by Tura et al. (2025). Specimen UWS1 was taller than specimens UW1 and UW2, with a net height of 4040 mm (excluding foundation and collar height), and the specimen incorporated two 100 mm-thick surrounding (outer) story slabs along its height. The wall unit was constructed on a 500 mm-thick rigid foundation affixed to the shake table. In order to support the masses attached to the top of the wall specimen, a U-shaped RC col-

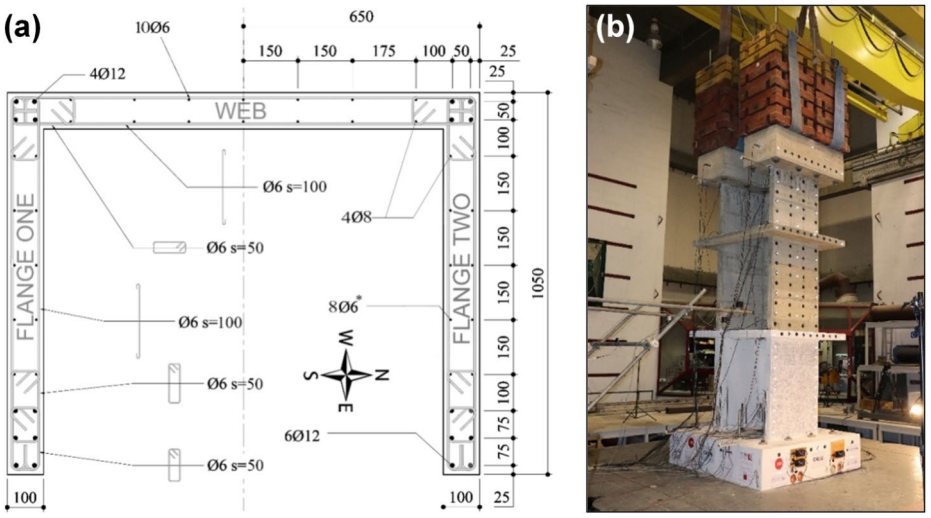

Fig. 9 Specimen UWS1; (**a**) wall cross-section, and (**b**) photograph of the specimen (Hoult et al. 2024). All dimensions are in mm

lar beam was constructed on top of the specimen, which was in the form of an extension of the U-shaped wall, along which the wall thickness was increased to 500 mm over a depth of 700 mm. The cross-sectional dimensions of the wall specimen (measured along outside faces) were 1050 mm parallel to the flanges, and 1300 mm parallel to the web, where the thickness of the wall was 100 mm. As shown in the cross-sectional view (Fig. 9a), the wall specimen had four confined boundary regions, two located at the flange free ends and the remaining two at the web-flange intersections.

The reported average concrete compressive strength for the wall specimen, obtained from test results on cylinder specimens, was 27.0 MPa. Results of the tensile stress–strain tests conducted on longitudinal reinforcing steel bar samples are presented in Table 1. The notations d_{bl},f_y,f_u, ε_{sy}, ε_{sh}, ε_{su}, and E_s in Table 1 refer to the diameter of the longitudinal reinforcing bar, yield strength, ultimate strength, yield strain, hardening strain, ultimate strain, and Young's modulus, respectively.

In order to enforce the specimen to exhibit nonlinear flexural behavior, additional masses with a total mass of 24.96tons were affixed to the top collar beam of the specimen. Combined with the approximate masses of the top collar beam (3.27tons) and the wall unit itself (4.17tons), the total mass of the specimen above the rigid foundation was 32.4tons. It must be noted that the specimen incorporated significant torsional eccentricity in the N-S direction according to the cardinal directions given in Fig. 9a, between its linear elastic shear center and the center of the additional mass sources, as well as the mass of the wall itself and the collar beam at the top.

For shake table testing of specimen UWS1, horizontal components of the ground accelerations corresponding to the largest event (M_w 6.5) of 2016 Central Italy earthquake sequence, recorded at station MZ04, were used. Ground motions used during the tests, namely the corrected ground motions, are a processed version of the original ground motion records, where similitude laws on the original record were applied (i.e., the time step of the records was shortened). The 2% damped acceleration and displacement spectra for the corrected ground motion components used in excitation of the specimen in the E-W (PGA: 0.81 g) and N-S (PGA: 0.64 g) directions (Fig. 9a) are shown in Fig. 10. The excitation protocol used during the test program consists of consecutive application of uni-directional and bi-directional excitations, with the increasing ground motion amplitudes (scale factors) listed in Table 2.

During the tests, the first major damage observed on the wall specimen was crushing of concrete at southwest web-flange intersection, during application of bi-directional excitation GM6 (Fig. 11a). During this excitation, maximum drift ratios measured on the wall were 1.65% in E-W direction and 0.65% in N-S direction, together with a maximum top twist rotation of 0.025 rad. Sliding shear at the base of the wall, along a crack at the wall-foundation interface (Fig. 11c), was also reported during this excitation, which may have triggered spalling of concrete at web-flange intersections, due to kinking of the longitudinal reinforcing bars in these regions. Further concrete crushing was observed in the south flange

Table 1 Reinforcing steel bar properties for specimen UWS1

d_{bl} (mm)	f_y (MPa)	f_u (MPa)	ε_{sy} (mm/mm)	ε_{sh} (mm/mm)	ε_{su} (mm/mm)	E_s (GPa)
6	577	623	0.0028	-	0.046	208
8	538	664	0.0027	0.024	0.120	196
12	580	690	0.0029	0.021	0.101	199

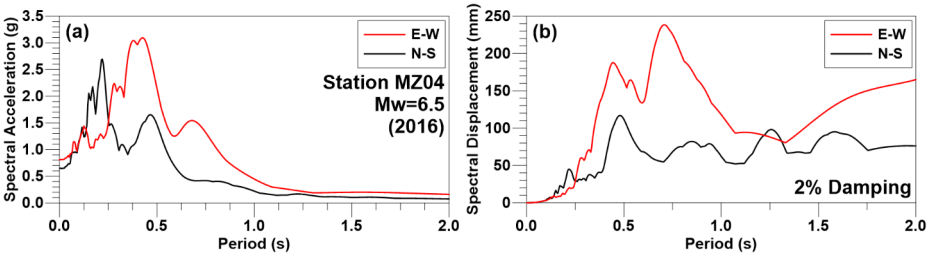

Fig. 10 Corrected ground motion (100% scale) used in shake table tests for specimen UWS1: (**a**) acceleration, and (**b**) displacement response spectra for 2% damping

Table 2 Corrected ground motion scale factors used in excitation of specimen UWS1

	GM0	*GM1*	*GM2*	*GM3*	*GM4*	*GM5*	*GM6*	*GM7*	*GM8*
E-W direction	10%	25%	25%	50%	50%	75%	75%	100%	100%
N-S direction	-	-	25%	0	50%	0	75%	0	100%

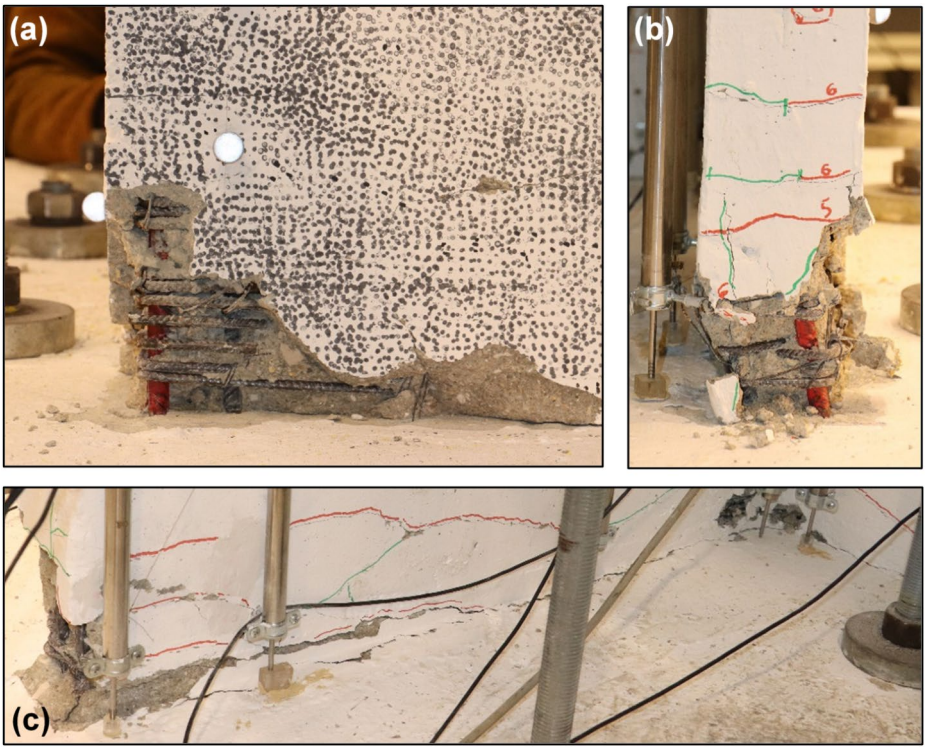

Fig. 11 Observed damage on specimen UWS1 (Hoult et al. 2024); (**a**) crushing of concrete at web-flange intersection, (**b**) crushing of concrete and buckling of reinforcement at flange free-end boundary region, and (**c**) wall-foundation interface crack at wall base

free-end boundary region, as well as at the web-flange intersections at both southwest and northwest corners of the wall specimen, under the uni-directional excitation GM7 (100%). During this excitation, the largest wall drift ratio was measured as 2.71% in E-W direction, and the sliding shear deformation at the base of the wall reached up to ±6 mm. Finally, during the last bi-directional excitation GM8 (100%), maximum drift ratios were measured as 1.82% in E-W direction and 0.76% in N-S direction, and the maximum top twist rotation was measured as 0.025 rad. This excitation caused concrete crushing in both of the flange free-end boundary regions, combined with noticeable buckling of longitudinal reinforcement in the south flange free-end boundary region (Fig. 11b) (Hoult et al. 2024).

The full-scale 10-story reinforced concrete building specimen tested at E-defense shake table facility in 2015, namely the E-defense 2015 specimen, is a wall-frame building-type structure with a total height of 25.9 m (Fig. 12c). As shown in the typical floor plan for the test building (Fig. 12a), plan dimensions are 12 m in one direction and 8 m in the other direction, and the lateral load resisting system of the building in the longer plan direction, namely the "frame direction", consists of moment resisting frames, whereas in the shorter plan direction, namely the "wall direction", the main lateral load resisting members are rectangular walls. Due to limitations of the shake table, structural walls in the building continued only up to the eighth floor level (8FL in Fig. 12b), and the structural system converts into moment resisting frames along the top three stories in the wall direction. The building incorporated three typical column sections, namely C1, C2, and C3, where C1 and C2 had cross sectional dimensions of 550 mm×550 mm, 550 mm×500 mm, and 500 mm×500 mm along the first story, second story, and the remaining stories of the building, respectively. On the other hand, column C3, which was designed as the boundary region of the structural walls, had cross sectional dimensions of 230 mm×450 mm along the entire building height. The width and depth of the beams varied from 230 mm to 350 mm, and 370 mm to 550 mm, respectively. The web thickness of the walls was 230 mm along the first six stories, reducing to 150 mm along the seventh story, and slab thickness at all floors was 120 mm. During the experimental campaign, the tests were performed under two different connection conditions between the foundation of the building and the shake table, in order to assess use of sliding bearings as a seismic mitigation technique. During the first stage of the test program,

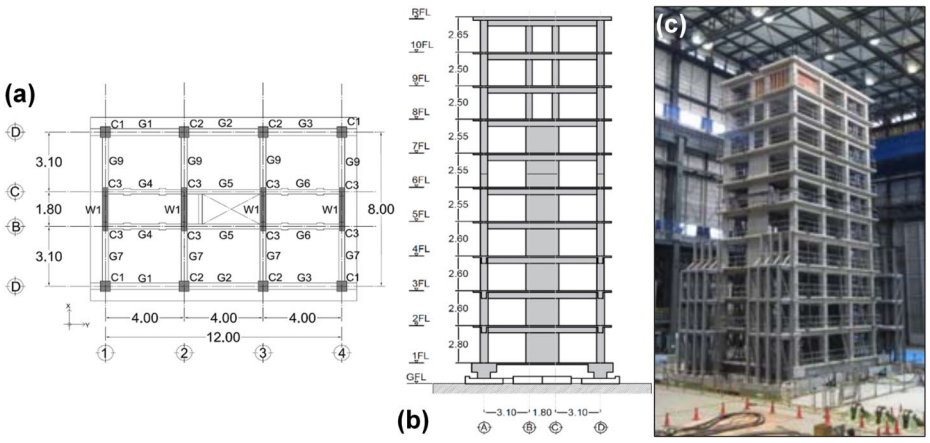

Fig. 12 Geometry of 2015 E-defense 10-story building specimen: (**a**) typical floor plan, (**b**) elevation view in wall direction, (**c**) photograph of the specimen (Kajiwara et al. 2021). All dimensions are in meters

Table 3 Concrete compressive strength test results for the E-Defense 2015 test Building

Story	1st	2nd	3rd	4th	5th	6th $_{lower}$	6th $_{upper}$	7th	8th	9th	10th
Testing Age (Day)	237	211	189	164	143	134	253	227	204	179	153
Test Strength (MPa)	68.7	72.0	57.6	48.1	45.5	42.1	54.6	49.0	51.9	43.9	41.0
Design Strength (MPa)	42.0	42.0	33.0	33.0	33.0	27.0	27.0	27.0	27.0	27.0	27.0

Table 4 Reinforcing steel bar properties for the 2015 E-Defense test Building

	d_{bl} (mm)	f_y (MPa)	f_u (MPa)	ε_{sy} (mm/mm)	ε_{sh} (mm/mm)	ε_{su} (mm/mm)	E_s (GPa)
SD295	10–16	370	515	0.0019	0.01	0.26	190
SD345	19–22	390	581	0.0021	0.01	0.23	190
KSS785	10	931	1100	-	-	0.12	205

which is referred to as the "base-slip" stage, sliding of the building on friction-type bearing elements was allowed. After completion of the first stage, the building was affixed to the foundation beams, and the ground motions were reapplied, during namely the "fixed-base" stage of the test.

The test building was designed in compliance with the Japanese Building Standard Law (AIJ, 2010) and the Japanese Structural Technical Standard Manual for Buildings (MLIT, 2007). Concrete strengths adopted in design were 42 MPa, 33 MPa and 27 MPa, varying among the stories. As shown in Table 3, material tests conducted on concrete samples provided higher compressive strengths than anticipated. In design and construction of the test building, three different steel grades, namely SD295, SD345 and KSS785, were used for reinforcing steel, for which average values of the mechanical properties obtained from reinforcing steel bar sample test results are listed in Table 4.

During the experimental program, the JMA-Kobe strong ground motion record, recorded at Kobe's Nakayama district during the 1995 Hyogo-ken Nanbu Earthquake, was used for excitation of the 10-story test building. All three components of the recorded ground accelerations were applied simultaneously, where the N-S component of the ground motion was oriented in the frame direction, and the E-W component was oriented in the wall direction of the test building. The excitation protocol of the test was sequential application of the recorded ground motion with increasing amplitudes (scale factors) of 10%, 25%, 50%, and 100%, during the base-slip stage, followed by the same amplitudes during the fixed-base stage. Lastly, an additional excitation was also applied, with a 60% scale factor, to represent possible aftershocks following a large earthquake. In this study, for analysis of the E-Defense 2015 test building, average base accelerations (PGA: 1.04 g in frame direction, 0.73 g in wall direction, and 0.43 g in vertical direction for 100% amplitude) that were recorded using the accelerometers located on the foundation level (base of columns and structural walls) of the building, are used. The reported maximum story drift ratios, in both the frame (0.60%) and the wall (0.30%) directions of the building, that were recorded during base-slip stage of the test were relatively small and did not cause notable damage on the specimen (Tosauchi et al. 2017). Within the scope of this study, only the fixed-base stage of the test program is simulated, for which significant maximum story drifts were reported (3.05% in frame direction, 1.50% in wall direction). The corresponding acceleration response spectra of the recorded foundation-level (building base) accelerations, generated for 2% damping

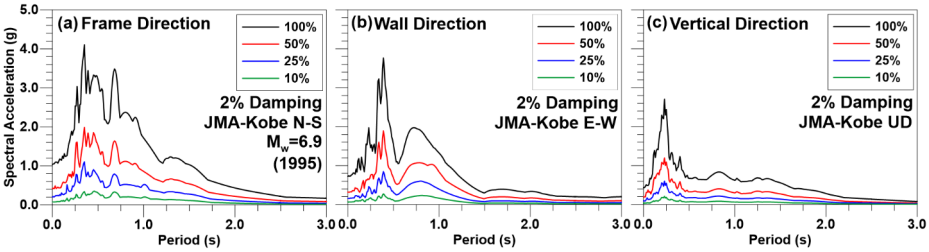

Fig. 13 Acceleration response spectra for the recorded ground accelerations at the foundation level of the E-Defense 2015 test building, during the fixed-base stage of the test: (**a**) in frame direction, (**b**) in wall direction, and (**c**) in vertical direction

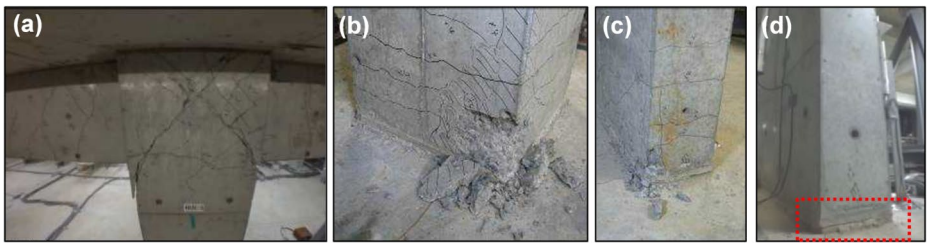

Fig. 14 Observed damage on the E-Defense 2015 test building; (**a**) flexural cracking of beams and damage on beam-column joints, (**b**) spalling of cover concrete at the base of a column, (**c**) minor spalling of cover concrete in wall boundary regions at the base, and (**d**) wall-foundation interface crack at wall base (Tosauchi et al. 2017)

ratio, are presented in Fig. 13 for 10%, 25%, 50%, and 100% amplitude excitations for the fixed-base stage of the test.

The most significant damage observed on the test building was shear damage to beam-column joints, where diagonal cracks were first observed during the 50%-amplitude fixed-base excitation, and widening of the cracks together with spalling of concrete was reported during the 100%-amplitude excitation. Furthermore, flexural cracks developing on the beams, together yielding of beam longitudinal reinforcement, was also observed (Fig. 14a). Limited concrete spalling was reported at the base of the columns and the structural walls, whereas flexural cracking was clearly observed on both (Fig. 14b, c). On the structural walls, horizontal interface cracks developing between the base of the walls and foundation the slab were detected, possibly stemming from yield penetration (extension/slip) effects on the wall longitudinal reinforcement within the foundation slab (Fig. 14d). Similarly to structural walls, interface cracks at base of columns were also observed.

4 Nonlinear dynamic response simulations

The dynamic response predictions presented in this section aim to demonstrate the overall dynamic response simulation capabilities of LFSAFE model, for both the isolated U-shaped wall specimen and the wall/frame test building investigated, under multi-directional and sequentially-applied seismic excitations. The accuracy of the LFSAFE models in predicting

the test results is not critically-evaluated, since other factors are also expected to influence the accuracy of the response predictions, including the damping ratio assumed in analysis, warping restraint imposed on the U-shaped wall by the collar beam, modeling approaches used for other structural components (beams and columns) in the test building, the effect of floor slabs on the response of the test building, the effect of previously-applied excitations (in the base-slip configuration), on the response of the test building, etc. However, discrepancies between the analytical response predictions and the test measurements are clearly identified, and possible reasons of these discrepancies are discussed.

4.1 Model generation methodology

Analysis models for specimen UWS1 and the E-Defense 2015 test building were generated in OpenSees, using the LFSAFE model elements for the walls. In generation of the analysis models, for consistency, a unified model calibration approach is adopted among the two specimens, which is the same calibration approach used in experimental validation studies presented in the companion paper by Tura et al. (2025). In the analysis model for specimen UWS1, model elements at wall boundary regions are discretized along wall length so that the length to thickness ratio of the shell elements do not exceed 2.0, which requires at least two model elements side-by-side for boundary regions with 300 mm length and 100 mm thickness. The same approach requires single model elements for the boundary regions of the rectangular walls (450 mm length and 230 mm thickness) in the E-Defense 2015 test building. However, due to the connecting frame elements in transverse direction of the walls at the midpoint of boundary regions, these regions are also modeled also using two model elements side-by-side. The model elements are then discretized across the entire wall geometry so that the height-to-length ratios of all model elements are close to one. Resulting model element discretization for specimen UWS1 and the walls in the E-Defense 2015 building specimen are presented in Fig. 15. For both specimens, the walls are divided into nine membrane layers across their thickness. These layers account for various concrete confinement and reinforcement characteristics, including two cover concrete layers (unconfined concrete with no reinforcement), two horizontal reinforcement layers (unconfined concrete with horizontal reinforcement only), two vertical reinforcement layers (confined concrete with vertical reinforcement only), and three core concrete layers (confined concrete with no reinforcement). Sensitivity studies conducted on the analysis results showed that using a finer model discretization did not result in notable difference in the model response predictions. In calibration of material model parameters, whenever material test results were available, constitutive material parameters of concrete and reinforcing steel are calibrated to match the test results. Otherwise, well-established empirical relationships are used to define the material parameters. For example, for specimen UWS1, parameters (modulus of elasticity, strain at peak stress and shape parameter) required for definition of the unconfined concrete stress–strain curve in compression are defined according to the empirical equations proposed in Chang and Mander (1994), since only average compressive strength of the concrete samples was reported. On the other hand, for the E-Defense 2015 test building, these parameters are calibrated so that that resulting monotonic compression envelope of the constitutive model for concrete matches with the reported stress–strain curves obtained from cylinder tests. Confined concrete behavior for both specimens are defined according to the confinement model by Mander et al. (1988), where the post-peak slope of concrete compression envelopes adopted for both unconfined and confined concrete are calibrated to match the post-peak slope of the Saatcioglu and Razvi (1992) model. Concrete tensile strength

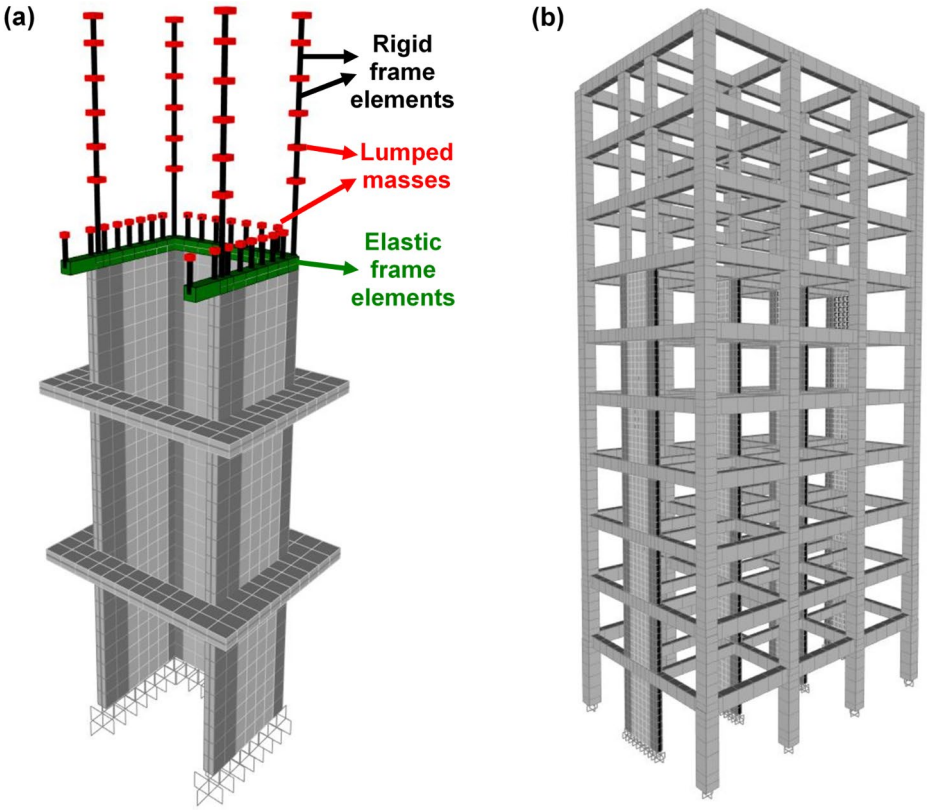

Fig. 15 OpenSees models generated for: (**a**) specimen UWS1, (**b**) E-Defense 2015 test building

and the corresponding tensile strain are defined as 0.31 $\sqrt{f'_c}$ and 0.00008, as proposed by Belarbi and Hsu (1994). The post-cracking stress–strain envelope for concrete in tension is also calibrated to agree with the equation by Belarbi and Hsu (1994). For reinforcing steel, tensile yield strength and tensile strain hardening ratio parameters are defined to agree with the steel stress–strain test results reported for both the UWS1 and E-Defense 2015 specimens. However, these parameters are modified, as described by Belarbi and Hsu (1994), to consider the effects of tension stiffening on reinforcing bars embedded in concrete. For representation of the Bauschinger's effect, hysteretic parameters describing the cyclic stiffness degradation characteristics of the constitutive relationships adopted for reinforcing steel are defined as R_0=20, a_1=18.5, and a_2=0.15, as recommended originally by Menegotto and Pinto (1973) and also adopted by Dhakal and Maekawa (2002a). Isotropic strain hardening is not considered in the constitutive relationships adopted for reinforcing steel. The friction coefficient in the constitutive model adopted for shear aggregate interlock along crack surfaces is defined as 0.40 (a value of 0.44 was recommended by Tassios and Vintzēleou 1987).

In terms of reproducing wall boundary conditions, the top collar beam of specimen UWS1 is included in the analysis model of the wall, using linear elastic frame elements (elements highlighted in green in Fig. 15a). The flexural stiffnesses (*EI*) of the frame elements used for the collar beam is amplified by a factor of 1000 in their major bending direction,

for eliminating very local vibration modes, since the top masses are attached rigidly to these frame elements. For the same reason, the torsional stiffnesses (GJ) of the frame elements located at the top of the wall flanges are also amplified by the same factor. Similarly to the collar-beam modeling approach adopted for the torsionally-loaded U-shaped wall specimen UW2 investigated in Tura et al. (2025), for the central frame element located at the top of the web of the wall specimen, an effective torsional stiffness of $0.05GJ$ is defined, in order not to fully restrain the torsional warping of the wall cross-section during the excitation. Furthermore, a rigid diaphragm constraint is defined at top of the wall specimen, for achieving more uniform load transfer in the region. The additional weights at the top of the wall, as well as the self-mass of the collar beam, are defined in the model as lumped masses (shown in red in Fig. 15a) at elevations corresponding to the mass centers. These masses are connected to the top collar beam elements using fully-rigid frame elements (shown in black in Fig. 15a). Furthermore, although not shown explicitly in Fig. 15a, lumped masses corresponding to the self-weight of the wall specimen are defined at the nodes of the model, based on the model element discretization and the corresponding tributary volumes of the model element nodes. Vertical (gravity) loads that are compatible with all nodal masses are also defined at corresponding nodes of the model. The flexural stiffness of the floor slabs surrounding the wall specimen at the first and second floor levels can potentially induce a coupling effect on the wall flanges (mostly flexural and to a lesser extent torsional, in the form of restraint against warping), which would influence the response of the wall in north-south direction, as well as its torsional response. Therefore, the floor slabs on the wall specimen are also modeled using LFSAFE model elements, so that their nonlinear out-of-plane behavior is considered in the analysis. Finally, fixed support conditions are defined at the wall-foundation interface, restraining all translational and rotational DOFs, similarly to the approach adopted in Tura et al. (2025).

In generation of the analysis model for the E-Defense 2015 test building, displacement-based beam-column elements (with three integration points) with fiber cross sections are used for modeling of the beams and columns. Discretization of the frame elements involves using at least six elements along the length of each member, also taking into account the expected plastic hinge lengths (half of the depth of cross section). The fiber cross sections are defined using 484 (22×22) concrete fibers for the columns and 66 (3×22) concrete fibers for the beams, also considering the confinement geometry of the cross sections. Similarly to the LFSAFE model elements employed for the walls, in the beam-column model elements, uniaxial behavior of the concrete and reinforcing steel fibers are defined employing the hysteretic material models by Chang and Mander (1994) and Menegotto and Pinto (1973). Buckling of reinforcement is not considered in the beam-column model elements. Material model parameters of the beam-column elements are calibrated using the same methodology adopted for the wall model elements. However, the effects of tension stiffening on the tensile yield strength and tension strain hardening ratio are not considered, since the relevant methodology (Belarbi and Hsu 1994) does not apply to frame element cross-sections. During the tests, significant shear damage was observed on the beam-column joints (due to joint shear), although in the frame direction of the building only. Since this study focuses on the response of the test building in the wall direction, and such beam-column joint damage influences the response of the building only in the frame direction, a nonlinear modeling approach is not adopted for the beam-column joint regions. Instead, beam-column joint flexibility is implicitly represented in the analysis model using elastic beam and column elements in

the joints, where the flexural stiffness of only the column elements only is amplified by a factor of 1000, as per the recommendation in ASCE 41 − 17 (2017) for beam-column joints satisfying the strong-column weak-beam condition. Presence of RC floor slabs, as well as their influence on the beams (i.e., increase in flexural stiffness and moment capacity) are neglected in the analysis model, and a rigid diaphragm kinematic constraint is applied at each floor level. However, since the beams in the building are modeled using beam-column elements with fiber sections, in order to eliminate the rigid diaphragm restraint against axial-growth in the beam elements, only the end nodes of the beam elements are connected to the rigid diaphragm, and an axial release is defined on the beam elements at mid-length, allowing axial elongation. Since floor slabs are not included in the analysis model, their self-weights are defined as distributed loads on surrounding beam elements. Since nonlinear dynamic analysis of the test building is conducted under three-directional excitation, to take into account the effects of vertical ground motion component on the response, the distributed mass of the building is defined as tributary lumped masses in all three directions. The tributary lumped masses are defined at the floor-level nodes of the wall and column model elements, which are connected to the rigid floor diaphragms. Distributed masses are not assigned along the length of the beam and column model elements, in order to eliminate very localized vibration modes, although the masses of all members are considered in the tributary lumped mass calculations. Fixed-support conditions are enforced at the base nodes of the column and wall model elements. The foundation slab of the building is not included in the analysis model, since the accelerations recorded at the top of the foundation are used in analysis. For analysis of both the U-shaped wall specimen UWS1 and the E-Defense 2015 test building, mass and stiffness proportional (Rayleigh) damping with 2.0% damping ratio (for the first and third vibration modes of the U-shaped specimen, and for the first and ninth vibration modes of the E-Defense 2015 test building) is defined. The 2.0% damping ratio was selected as an approximate value, and was adopted for both the isolated wall and wall-frame system, for the sake of consistency. Naturally, the real damping characteristics of two specimens may differ.

4.2 Dynamic response simulations for the U-Shaped wall specimen

The uni-directional and bi-directional shake table tests conducted on the isolated U-shaped wall specimen UWS1 are first simulated in OpenSees, using the LFSAFE model elements for the wall. The excitation protocol applied during testing is replicated by application of the nine consecutive ground motion records on the analysis model. Model predictions for the global response quantities of the specimen are compared with experimental measurements, in terms of top displacement, top twist rotation, and story acceleration response histories. Furthermore, representative local deformation predictions of the model for the average longitudinal strains at the base of the wall and the shear distortions (average shear strains) on a wall flange along the first story height of wall are compared with test measurements. Model predictions for the displacement, twist rotation, and story acceleration response histories are presented only for the last four excitations (GM5, GM6, GM7 and GM8), focusing on the response under relatively large ground motion amplitudes applied both uni-directionally and bi-directionally. Representative local deformation comparisons of model predictions (or post-dictions obtained using an updated model configuration) and test measurements are provided only for the uni-directionally applied ground excitations GM5 and GM7.

A representative deformed shape (using an amplification factor of 12.0) obtained from the analysis of specimen UWS1, corresponding to a time instant with large lateral displacement and top twist rotation demands experienced during the bi-directional excitation GM8 (at 8.245s), is presented in Fig. 16. The red lines in the figure represent the undeformed shape of the specimen. The analytically-obtained deformed shape clearly demonstrates the lateral displacements in both directions of the wall, as well as torsional twisting of the wall, indicating a combined flexural/torsional response. Warping of the wall cross section under torsion is also visible in the deformed shape. It must be noted that not imposing torsional cracking on the middle segment of the U-shaped collar beam (a cracked torsional stiffness of $0.05GJ$ is presently imposed) would have restrained warping of the wall cross-section at the top, almost to full extent.

Comparison of test measurements with model predictions for the top displacement time history responses of specimen UWS1, in the E-W direction under the uni-directional excitations GM5 (75% amplitude) and GM7 (100% amplitude), and in both E-W and N-S directions under the bi-directional excitations GM6 (75% amplitude) and GM8 (100% amplitude) are provided in Fig. 17. As demonstrated in Fig. 17a, b, under the uni-directional excitations GM5 and GM7, the LFSAFE model slightly underestimates the measured peak top displacement values, yet well-replicates the time instants of the peaks, capturing the vibration frequency (period) of the response. The model's capability in simulating the response of the non-rectangular wall under bi-directional excitation is demonstrated in Fig. 17c, d, e, f. The model well-replicates the test measurements under the 75% amplitude (GM6) and 100% amplitude (GM8) excitations, while slightly underestimating peak displacement values in the E-W direction only during the 75% amplitude excitation. In the N-S direction, the model response is accurate during the 100% amplitude excitation, with some discrepancy between model results and test measurements observed during the 75% amplitude excitation, after the third major displacement cycle (Fig. 17e, f). The experimentally-observed sliding shear deformation at the base of the wall, along horizontal cracks that developed at the flange-

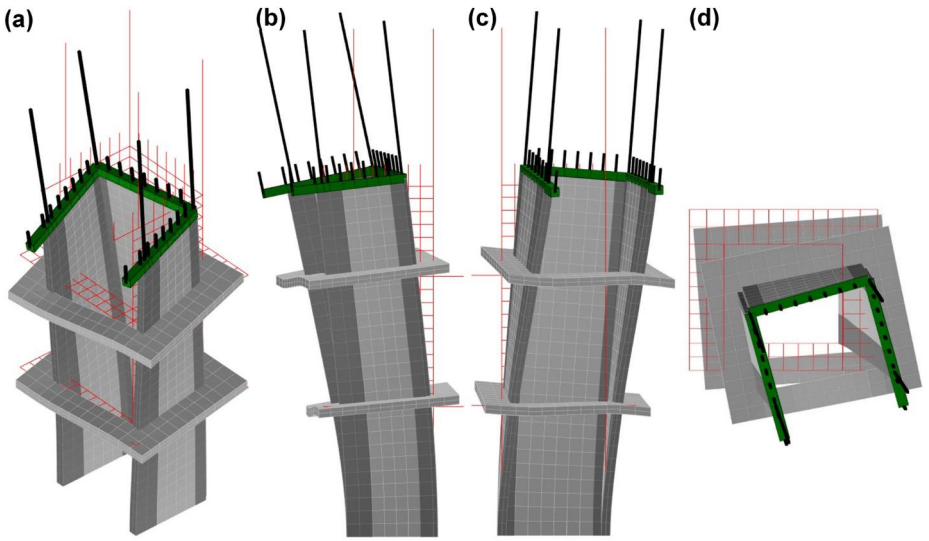

Fig. 16 Representative deformed shape obtained from analysis of specimen UWS1; (**a**) 3D view, (**b**) north side view, (**c**) east side view, and (**d**) top view

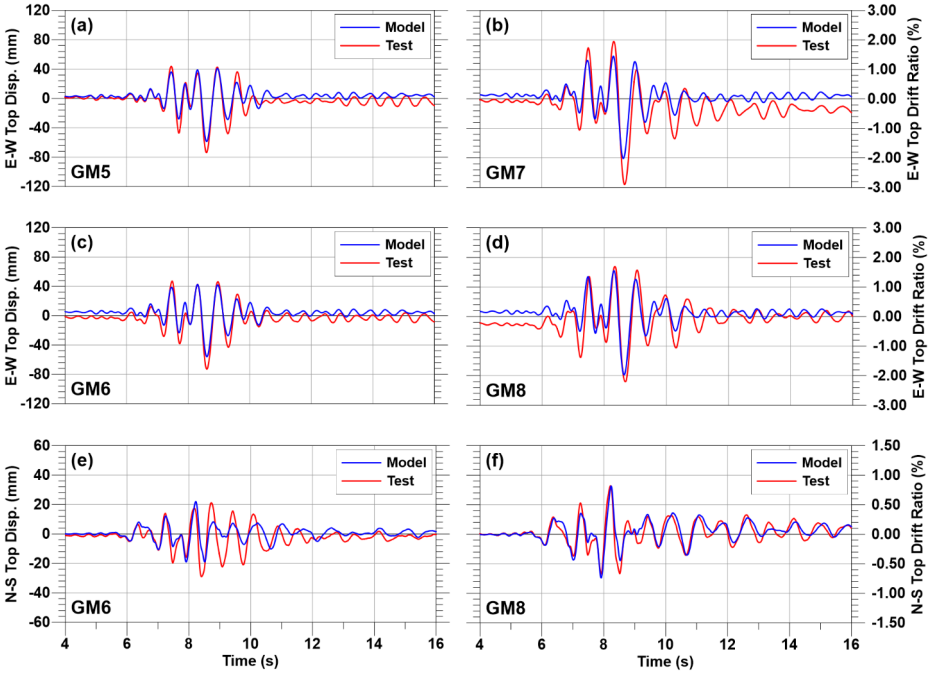

Fig. 17 Top displacement time histories for specimen UWS1: (**a**) in E-W direction, under uni-directional GM5, (**b**) in E-W direction under uni-directional GM7 (**c**) in E-W direction under bi-directional GM6, (**d**) in E-W direction under bi-directional GM8, (**e**) in N-S direction under bi-directional GM6, and (**f**) in N-S direction under bi-directional GM8

foundation interfaces, cannot be simulated by the analysis model, since the model formulation does not allow formation of a continuous crack across the wall cross-section. This may have possibly caused underestimation of the top displacement values measured in the E-W direction of the wall. Furthermore, the damping ratio assumed in analysis (presently 2.0%) is also expected to have an influence on the analytical response predictions, making a critical assessment of the model accuracy difficult, as applies to all model response predictions presented henceforth.

Comparison of model predictions with the experimentally-measured top twist rotation time histories of specimen UWS1, under bi-directional 75% (GM6, Fig. 18a) and 100% (GM8, Fig. 18b) excitations, demonstrates the capability of the LFSAFE model in simulating the torsional deformations developing on a U-shaped wall. Despite moderate underestimation of the test measurements after the fourth major twist cycle, the model captures the peak top twist rotation values that were measured during both excitations.

Performance of the LFSAFE model in reproducing the acceleration response histories measured along the height of the U-shaped wall specimen under uni-directional (Fig. 19a, b) and bi-directional (Fig. 19c, d,e, f) excitations with 75% and 100% amplitudes, is evaluated in Fig. 19. The experimentally-measured floor accelerations presented in Fig. 19 were obtained after post-processing of the test data, via application of a band-pass filter with 0.25 Hz and 10 Hz limit frequencies. Under uni-directional excitations, the model reasonably predicts the measured acceleration time histories at the first and second floor levels,

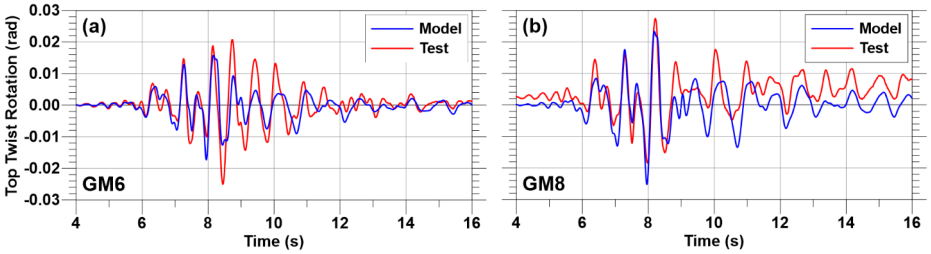

Fig. 18 Top twist rotation time histories of specimen UWS1 under bi-directional excitations: (**a**) GM6, and (**b**) GM8

including the peak acceleration values. However, at the top floor level, although model predictions are reasonable in the positive E-W direction, the model overestimates the peak acceleration values measured in the negative E-W direction (Fig. 19a, b). Similarly, under the bi-directional excitations, the model reasonably estimates the accelerations measured at the first and second floor levels, while it slightly overestimates the accelerations at the third-floor level, in both N-S and E-W directions (Fig. 19c, d,e, f). Subject to uncertainties associated with damping, boundary conditions (e.g., top collar beam stiffness), and unexpected failure/behavior modes (e.g., sliding shear at wall base), response comparisons presented in this section demonstrate the effectiveness of the model in reasonably simulating the global dynamic response characteristics of a U-shaped wall subjected to both uni- and bi-directional ground motions, in terms of acceleration, lateral displacement, and twist rotation response histories.

For evaluating the capabilities of LFSAFE model in simulating local (deformation) responses, average longitudinal strains measured using vertical displacement sensors (LVDTs) with 70 mm gauge lengths installed at the base of the wall at the south flange end (LVDT13 in Fig. 20) and at the south web-flange intersection (LVDT04 in Fig. 20), as well as the wall flange shear distortions measured using diagonally-oriented spring potentiometers installed along the first story height of the wall specimen (Fig. 20), are compared with model predictions in Figs. 22 and 23, respectively, under ground excitations GM5 and GM7. Comparisons presented in these figures clearly reveal that the "original" model configuration drastically underestimates both the experimentally-measured average vertical strains at the base of the wall and the wall flange shear distortions measured along the first story height of the wall.

Similarly to very recent studies presented in the literature on modeling of specimen UWS1 (Hoult and Almeida 2024), sensitivity studies conducted using the LFSAFE model for the U-shaped wall specimen have revealed that local deformation estimations of the model are influenced by consideration of strain penetration effects in modeling and the damping ratio assumed in analysis. Since in the original model configuration, the foundation of the wall, the wall-foundation interface, and the strain penetration effects on the longitudinal reinforcing bars in the foundation were not considered, an "updated" (manipulated) model configuration for the wall specimen was generated, and the aforementioned local deformation measurements were compared with results of the updated model also. In the updated model configuration, the damping ratio was reduced from 2.0% in the original model to a value 0.25%, similarly to the damping ratio adopted in the local deformation post-diction studies conducted for the wall specimen in the paper by Hoult and Almeida

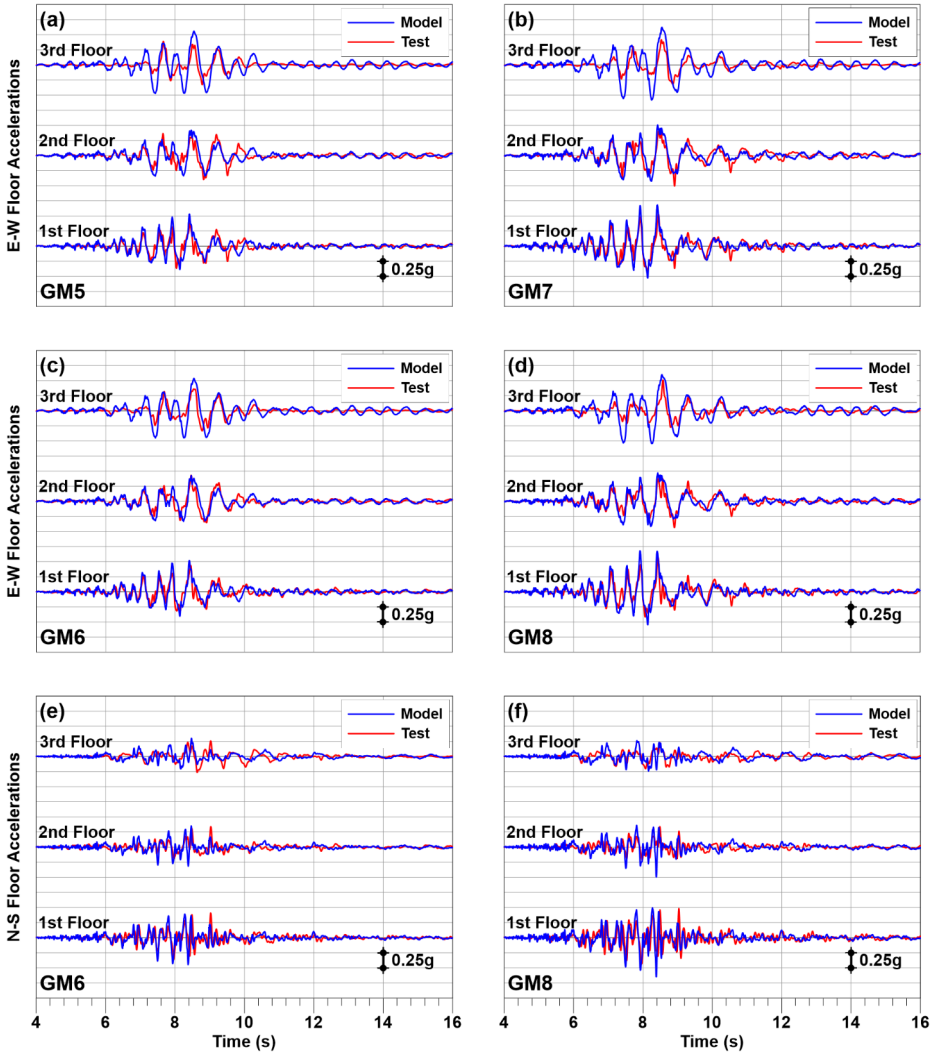

Fig. 19 Floor acceleration time histories of specimen UWS1: (**a**) in E-W direction, under uni-directional GM5, (**b**) in E-W direction under uni-directional GM7 (**c**) in E-W direction under bi-directional GM6, (**d**) in E-W direction under bi-directional GM8, (**e**) in N-S direction under bi-directional GM6, and (**f**) in N-S direction under bi-directional GM8

(2024), and strain/yield penetration effects were considered in modeling using an indirect (macroscopic) modeling approach similar to that adopted in the same paper.

In this macroscopic modeling approach, extension/slip deformations that develop on the longitudinal reinforcing steel bars within the foundation and accumulate at the wall-foundation interface (i.e., strain/yield penetration effects) are represented in the form of average tensile strains that develop within an additional row of LFSAFE model elements, which are defined directly below the wall-foundation interface (Fig. 21). The model nodes at the wall-foundation interface are restrained from horizontal displacements only, and the model

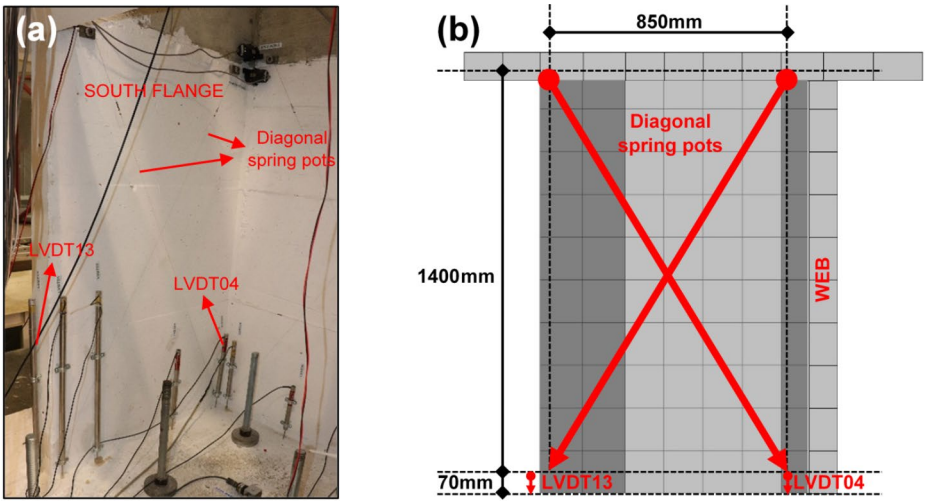

Fig. 20 Instrumentation for wall deformation measurements: (**a**) displacement sensors on the specimen (modified from Hoult et al. 2024), (**b**) sensor layout

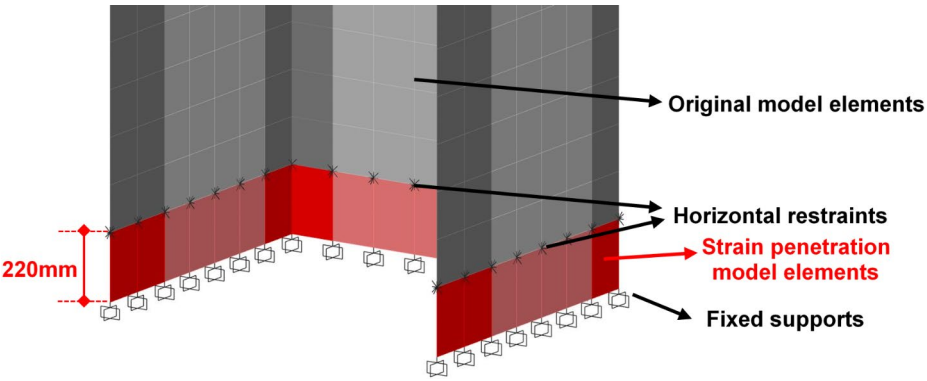

Fig. 21 Macroscopic modeling approach for consideration of strain penetration effects

elements representing the foundation (i.e., the depth of the foundation along which constant longitudinal tensile strains can be assumed) are assigned zero concrete tensile strength (for allowing tensile strains to freely develop along this depth) and approximately linear elastic stress-strain behavior for concrete in compression (for representing the relatively rigid behavior of the foundation under compression). For specimen UWS1, the height of these additional model elements (i.e., the strain penetration depth) is defined as 220 mm, as recommended by Hoult et al. (2022) based on strain gauge measurements on the reinforcing steel bars within the foundation of the U-shaped wall specimens UW1 and UW2, which were tested under quasi-static loading (Hoult et al. 2023a).

Average longitudinal strain time histories at wall base (along 70 mm gauge length) at the south flange end (Fig. 22a, b) and the south flange-web intersection (Fig. 22c, d) of the wall, obtained using both the original and updated model configurations, are compared with

test measurements in Fig. 22 under uni-directional excitations with 75% (GM5) and 100% (GM7) amplitudes in E-W direction. Notable improvement is observed in especially the tensile strain predictions obtained using the updated model. In the updated model results shown in Fig. 22, compared to the original model results, approximately 20% of the increase in the maximum tensile strain predictions is associated with the reduced damping ratio, whereas the remaining 80% is associated with consideration of strain penetration effects in the analysis. However, even with both modifications to the model, the measured tensile strains are still moderately underpredicted at the south flange end, under both excitations (Fig. 22a, b). At the south web-flange intersection of the wall, tensile strains estimated using the updated model are very close to the test measurements under excitation GM5, while the updated model still underpredicts, to a moderate extent, the maximum tensile strains measured at the web-flange intersection under excitation GM7 (Fig. 22c, d). The reason why the both the original and updated models drastically underestimate the measured compressive strains at the south flange end of the wall (especially under excitation GM7, Fig. 22b) is uncertain, and may be associated with the somewhat unexpected concrete crushing and out-of-plane buckling/instability failure observed at the south flange free-end. At this location, the experimentally-measured compressive strains were very large in magnitude, reaching 0.039 (Fig. 22b).

Shear distortions (average shear strains) measured along the first story height of the south flange of the wall are compared with results of both the original and updated model configurations in Fig. 23, under the uni-directional excitation GM7 (100% amplitude) in E-W direction only, since the corresponding test data under excitation GM5 was nonsensical. Both experimentally-measured and analytically-predicted shear distortions are calculated using the procedure described by Thomsen and Wallace (1995), based on the measurements obtained from the diagonal spring potentiometers (Fig. 20), and the nodal displacements in the analysis model corresponding to the diagonal sensor attachment points. Comparisons presented in Fig. 23 reveal that while the original model configuration underestimates the experimentally-measured shear distortions in both positive and negative directions, the

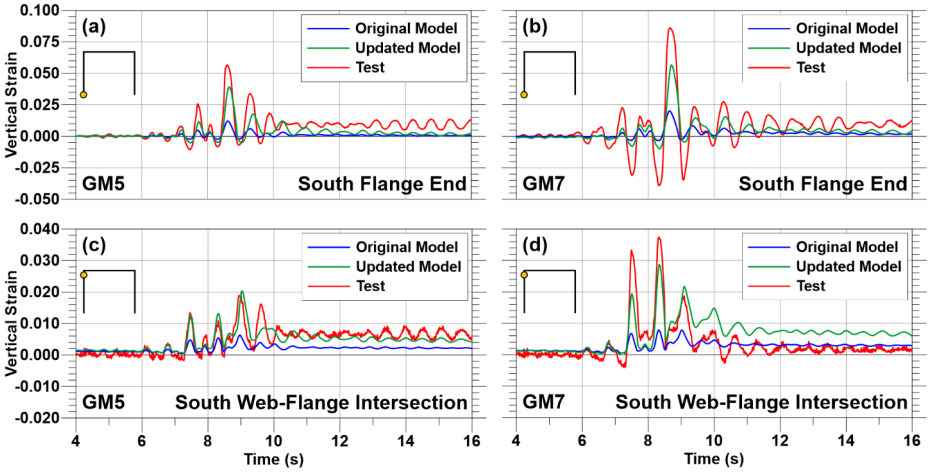

Fig. 22 Vertical strain time histories of Specimen UWS1: (**a**) at south flange end under uni-directional GM5, (**b**) at south flange end under uni-directional GM7, (**c**) at south web-flange intersection under uni-directional GM5, and (**d**) at south web-flange intersection under uni-directional GM7

updated model well-predicts the measured shear distortions in the positive direction, while it overestimates the measured shear distortions in the negative direction. In the updated model results presented in Fig. 23, compared to the original model results, approximately 35% of the increase in the maximum shear distortion predictions is related to reduction of the damping ratio, while the remaining 65% is associated with consideration of strain penetration effects in modeling. Consideration of strain penetration effects results in larger shear distortion predictions along the first story height of the wall, since smaller flexural deformations are predicted in this region (i.e., along the gauge length of the diagonal potentiometers, which do not straddle the wall-foundation interface).

Overall, for the U-shaped wall specimen, recalibration of the damping coefficient (from 2% in the original model to 0.25% in the updated model) together with consideration of strain penetration effects in the analysis (albeit indirectly and using a macroscopic approach) have improved the model post-dictions for the average tensile strains developing at the base of the wall and the shear distortions developing on a wall flange. However, although not shown here for brevity, these modifications have not significantly influenced the global response estimations of the model under large-amplitude excitations (displacement, twist angle, and acceleration response histories presented in Figs. 17, 18 and 19), to the extent that global response prediction capabilities of the model need to be re-evaluated.

In the analytically-predicted response of the U-shaped wall specimen UWS1, the experimentally-observed crushing of cover concrete and flexural yielding of longitudinal reinforcement at the flange free-end boundary regions of the wall are reproduced. However, out-of-plane buckling of longitudinal reinforcement at the south flange free-end of the wall is not captured in the analysis results. Furthermore, since the model is incapable of simulating sliding shear deformations developing along a continuous horizontal crack at the wall-foundation interface, the experimentally-measured sliding shear deformations and the experimentally-observed crushing of concrete at the web-flange intersections of the wall (which is believed to be associated with the kinking of the longitudinal reinforcing bars due to sliding shear deformations at the base of the wall), are not replicated in the response simulations. Overall, the model predicts a nonlinear flexural response for the wall specimen,

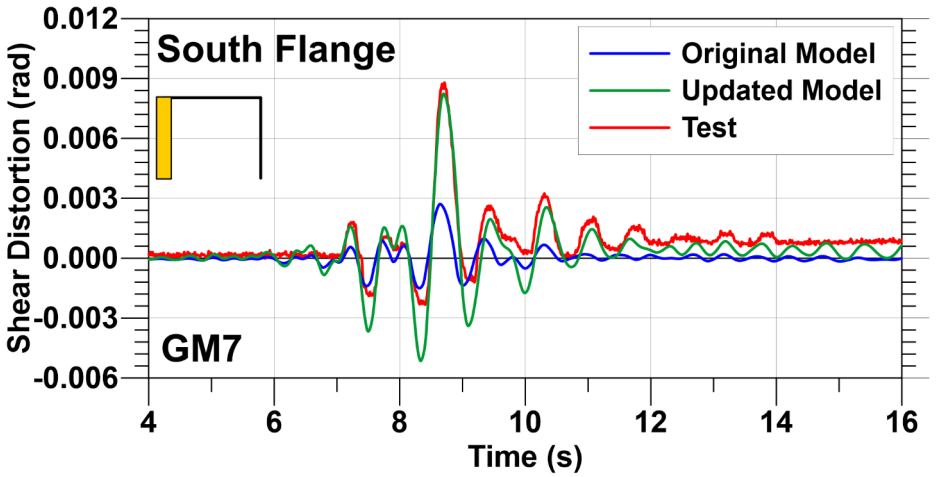

Fig. 23 Shear distortion time histories of specimen UWS1 at south flange under uni-directional GM7

with yielding of longitudinal reinforcement and crushing of cover concrete, which was the predominant behavioral mode of the test specimen, while it fails to capture the experimentally-observed sliding shear at the base of the wall and the out-of-plane buckling/instability failure at the south-flange free-end boundary region of the wall. It is possible that the sliding shear deformations observed during testing at the wall-foundation interface have triggered instabilities at the wall flanges (such as imperfect crack closure and kinking of longitudinal bars), leading to somewhat premature crushing of concrete together with buckling of longitudinal reinforcement at the flange free-end boundary regions, leading to the excessively large compressive strain measurements shown in Fig. 22b.

4.3 Dynamic response simulations for the 10 story wall-frame test building

Dynamic response prediction capabilities of the LFSAFE model are further evaluated via simulation of the E-Defense 2015 shake table tests conducted on a 10-story wall-frame building specimen. Nonlinear response history analysis of the building is conducted in OpenSees under the four consecutive three-directional ground acceleration record sets (corresponding to 10%, 25%, 50%, and 100% amplitudes) applied during the fixed-base stage of the test program. Since the primary focus of this simulation is to evaluate the performance of the LFSAFE model, analytical response predictions are compared with test results in the wall direction of test building only. For brevity, response comparisons are presented only for the 50% and 100% amplitude excitations. Model response predictions are compared with test measurements in terms of both global (displacements, accelerations, story drift ratios, base shear forces, base overturning moments) and local (wall base rotations, wall shear deformations, beam end rotations, column base rotations) response characteristics.

A representative deformed shape of the building (with an amplification factor of 20.0) obtained using the analysis model is shown in Fig. 24, at a time instant corresponding to relatively large lateral displacement demands (5.9s of the 100% amplitude excitation). In the figure, red lines correspond to the undeformed shape of the building. The deformed shape shows that the fundamental deformation mode of the test building is bi-directional translation, with no significant torsional deformation observed in the analysis results, which agrees with the test measurements. The structural walls are subjected to displacement demands along their in-plane (Fig. 24b) and out-of-plane (Fig. 24c) directions, simultaneously. Furthermore, the deformed shape presented in Fig. 24b reflects the contribution of frame action (wall-frame interaction) on the response of the test building. Moreover, concentration of flexural deformations on the beam plastic hinge regions can be observed in Fig. 24b.

Story displacement estimations of the analysis model presented in Fig. 25 for the 50% and 100% amplitude excitations indicate that the experimentally-measured story displacement amplitudes are predicted with reasonable accuracy, while they are slightly underestimated at lower floors levels. The time instants of the displacement peaks at all floor levels, as well as the frequency characteristics (vibration period) of the responses, are mostly well-captured. When the corresponding maximum story drift profiles shown in Fig. 26 are compared, significant underestimation of the maximum story drift ratios along the first story is observed during both excitation amplitudes. The horizontal cracks detected at the wall-foundation interfaces of the test building indicate that the longitudinal bars in structural walls may have been subjected to notable strain penetration effects, which may have decreased the flexural stiffness of the walls and led to underestimation of floor displacements and story drifts espe-

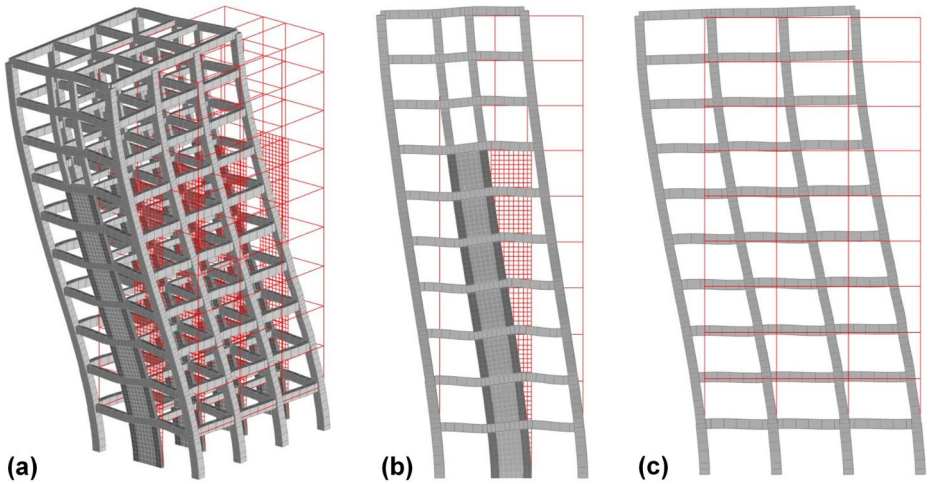

Fig. 24 Deformed shape of E-Defense 2015 specimen; (**a**) 3D view, (**b**) elevation view in wall direction, and (**c**) elevation view in frame direction

cially along the lower stories of the building, where wall flexural stiffness is more influential on the lateral stiffness of the entire structure. In contrast, overestimation of story drift ratios along the upper stories of the building may be related to neglecting, the analysis model, the contribution of the floor slabs on the lateral stiffness of the building (i.e., the flexural stiffness of the beams), since the stiffness associated with frame action has a more dominant influence on the dynamic response of the upper stories. It must be noted that accuracy of the model response predictions is also subject to other assumptions used in modeling and analysis, such as the assumed damping ratio, modeling approaches used for the beams and the columns, and neglecting the previously-applied excitations in the base-slip configuration of the test building. Uncertainties associated with these assumptions, and their influence on the accuracy of analysis results, apply to all response comparisons presented in this study for the test building.

Comparison of analytically-obtained floor acceleration time histories with test results presented in Fig. 27 show that the analysis model underestimates the accelerations measured at the upper floor levels (especially the top three floor levels) during both 50% and 100% amplitude excitations. The model reasonably captures the vibration frequency of the responses, and well-predicts the time instants at peak amplitudes, as was also the case in the story displacement predictions. Underestimation of floor accelerations along the upper three stories, where the walls are discontinued and lateral load resistance is due to moment resisting frame action only, may be directly associated with neglecting, in the analysis model, the contribution of floor slabs to the flexural stiffness (and flexural capacity) of the beams, and therefore their contribution to frame stiffness and strength.

Predicted and measured overturning moment vs. roof drift ratio response comparisons for the test building are presented in Fig. 28. Overturning moments in both test measurements and analysis results are obtained by first calculating first the floor-level inertial forces, by multiplying story accelerations with corresponding story masses, and then calculating the cumulative overturning moment of the inertial forces at the base of the structure. The

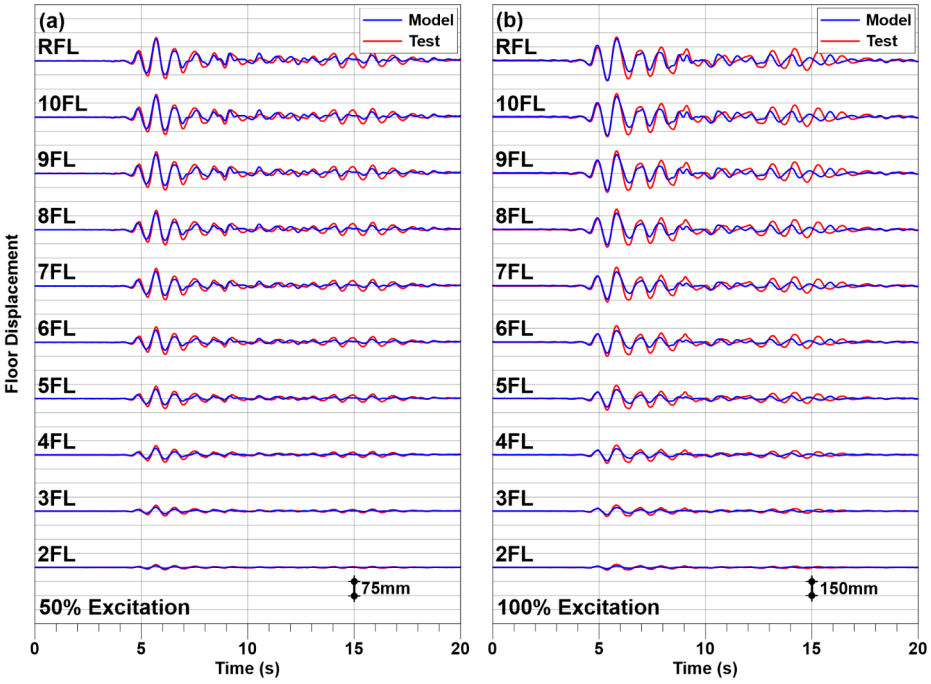

Fig. 25 Story displacement time histories of 10-Story E-Defense test building in wall direction under; (**a**) 50%, and (**b**) 100% excitations

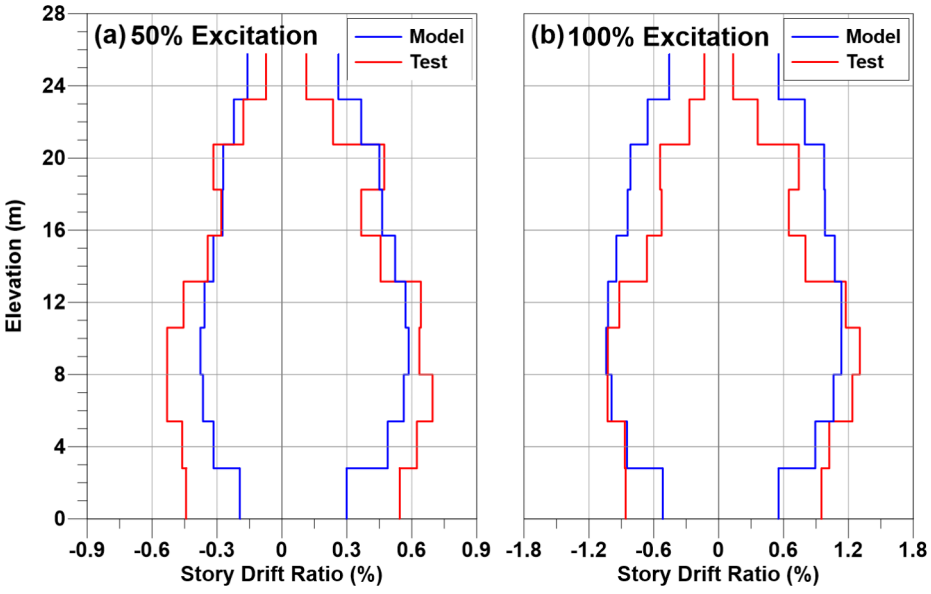

Fig. 26 Story drift profiles of the E-Defense test building in wall direction under; (**a**) 50%, and (**b**) 100% excitation

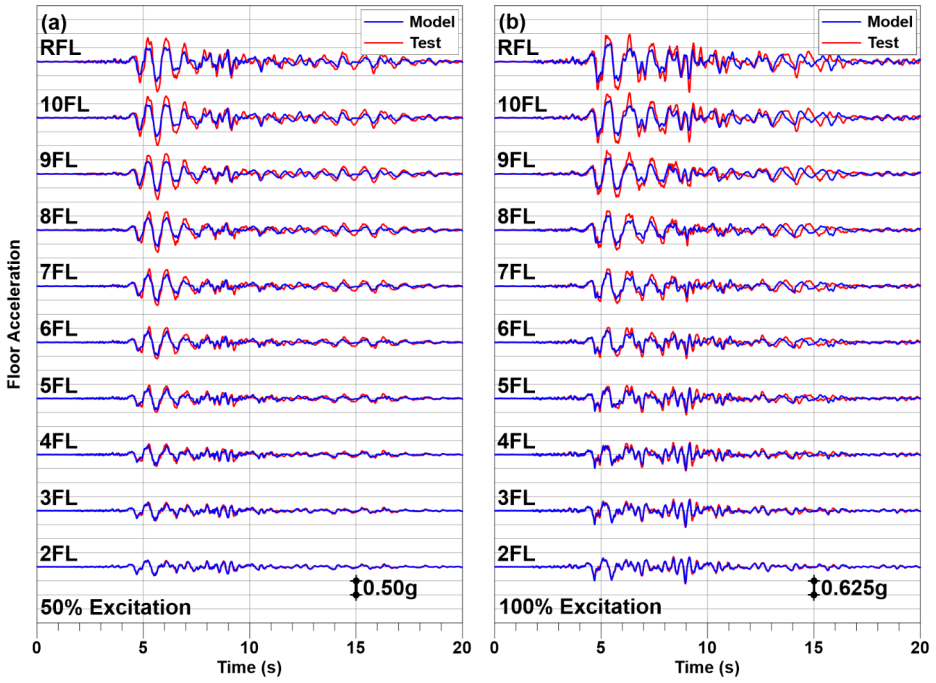

Fig. 27 Story acceleration time histories of the E-Defense test building in wall direction under; (**a**) 50%, and (**b**) 100% excitation

roof drift ratio is simply the top floor displacement divided by the total height of the building. Using this procedure, a hysteretic response for the whole test building is generated. This response is not identical the quasi-static response of the structure, since the influence of damping forces are also included in the floor-level inertial forces and therefore the overturning moment. Instead of base shear, overturning moment was considered in this hysteretic response comparison, since the base shear vs. roof drift response is influenced much more by the contribution of higher modes of vibration on the response. Comparison of the analytical and experimental overturning moment vs. roof drift responses presented in Fig. 28 reveals that underestimation of floor accelerations (especially along the top three stories of the building, Fig. 27), results in a more pronounced underestimation of the overturning moments at the base of the building. This is because the contribution of upper-floor accelerations to the overturning moment is much more pronounced, due to the larger moment arms of the upper floors with respect to the base. On the other hand, roof drift ratios predicted by the model, under both 50% and 100% amplitude excitations, are reasonably accurate.

Underestimation of story accelerations shown in Fig. 27 (possibly due to negligence of the floor slabs in modeling) has the same influence on the base shear time history predictions of the analysis model (Fig. 29). Experimentally-obtained base shear amplitudes are underestimated by the model during both excitations, although to a lesser extent when compared with the base overturning moments (Fig. 28). In both the experimental analytical results used in this comparison, base shear is calculated as the resultant of the story inertial forces. As was observed in both story acceleration and story displacement time histories, the model

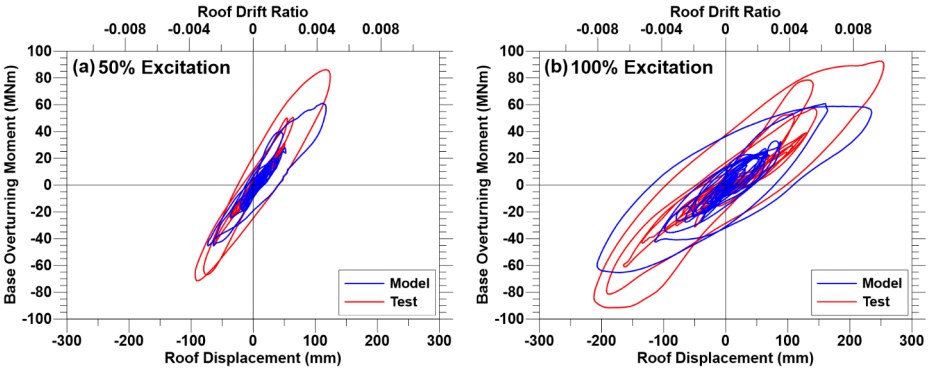

Fig. 28 Base overturning moment vs. top displacement response of the E-Defense test building in wall direction under (**a**) 50% and (**b**) 100% excitation

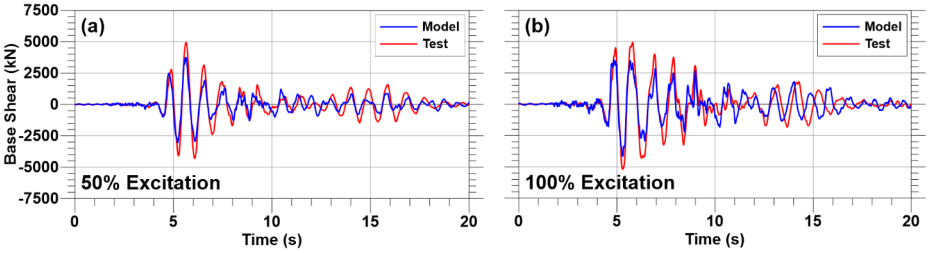

Fig. 29 Base shear time history of the 10-Story E-Defense test building in wall direction under: (**a**) 50%, and (**b**) 100% excitation

reasonably captures time instants of the base shear peak values, and the frequency characteristics of the response.

In order to investigate the influence of the flexural strength and stiffness characteristics of the floor slabs on the analysis results (story acceleration, base overturning moment, and base shear response predictions in particular), an alternative model configuration is generated, using a very simple and macroscopic approach for considering the contribution of the floor slabs. In this model configuration, the beams of the test building are not modeled as rectangular fiber cross-sections but instead as T-shaped fiber cross-sections, where the beam effective flange widths are defined as recommended in ASCE41-23 (2023). Compared to the original model results (Figs. 27b, 28b and 29b), the new model provides improved response predictions for the floor accelerations (Fig. 30a, especially along the upper three stories of the building, where the walls are discontinued lateral load resistance is due to moment resisting frame action only) and the base shear response history of the building (Fig. 30b). Furthermore, in the new model results (Fig. 30c), the pronounced underestimation of the base overturning moments obtained using the original model (Fig. 28b) is eliminated. It must be noted that this model configuration with the flanged beam cross-sections was used for presenting the analysis results shown in Fig. 30 only, for demonstration purposes.

As a local response (deformation) comparison, relative rotations measured along two regions (Fig. 31) along the first story height of a rectangular wall in the test building (wall

W1 along axis 1, Fig. 12a), are compared with model predictions in Fig. 32. Wall rotation measurements are obtained from vertical displacement sensors (LVDTs) shown in Fig. 31, where relative rotations along the gauge length of the displacement transducers are calculated by dividing the difference in the elongation or shortening measurements, divided by the horizontal distance between the sensors. The analytical wall rotations are obtained using the same procedure, using the vertical displacements at the model nodes corresponding to the points of attachment of the transducers. Relative rotation time history comparisons are presented along two gauge lengths, (W11L and W11U in Fig. 31a) under 50% (Fig. 32a) and 100% (Fig. 32b) amplitude excitations. Wall relative rotation predictions of the analysis model well-represent the test measurements, in terms of both the peak amplitudes and the response history, along the upper 2.2 m of the first story height (W11U), under both excitation levels. In contrast, peak amplitudes of the wall base rotations measured along the bottom 0.6 m of the first story height (W11L) are clearly underestimated. Similarly to the U-shaped wall specimen UWS1, this discrepancy may be partially related to the horizontal cracks that were detected at the wall-foundation interfaces of the test building, and the associated strain penetration (slip/extension) effects on wall longitudinal reinforcement. To further investigate this issue, an updated model configuration is also generated for the E-Defense test building, where strain penetration effects on wall longitudinal reinforcement are indirectly considered in modeling, utilizing the same macroscopic modeling approach that was adopted for the U-shaped wall specimen UWS1 (Fig. 21). An additional row of LFSAFE model elements, with zero concrete tensile strength and approximately linear elastic stress–strain behavior for concrete in compression, are defined directly below the wall-

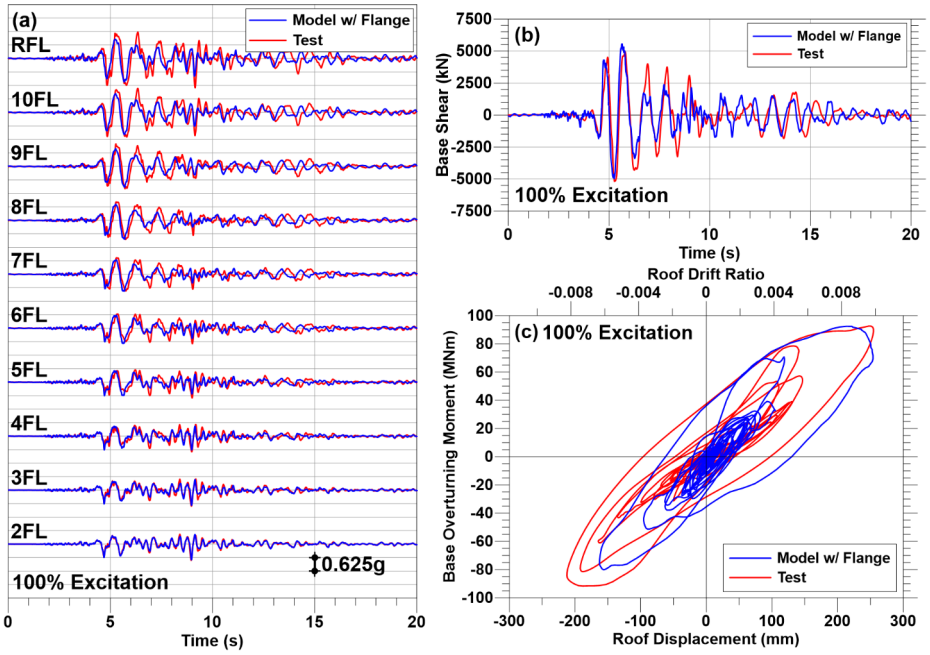

Fig. 30 Response predictions obtained using a modified model configuration with flanged beam cross-sections under 100% excitation: (**a**) story acceleration time histories, (**b**) base shear time history, and (**c**) base overturning moment vs. roof displacement response

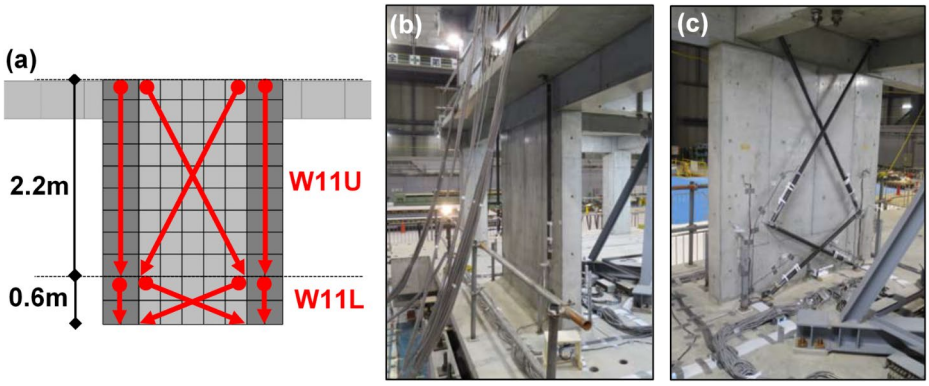

Fig. 31 Instrumentation for wall deformation measurements (Kajiwara et al. 2021)

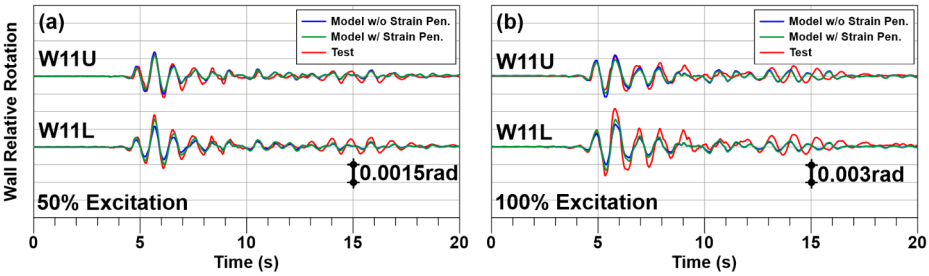

Fig. 32 Wall relative rotation time histories for the E-Defense test building under: (**a**) 50%, and (**b**) 100% excitation

foundation interfaces. The height of these additional model elements is defined as 190 mm, corresponding to the strain penetration depth of the longitudinal reinforcing steel bars in the wall boundary regions. This strain penetration depth is determined by first calculating the cumulative slip/extension of the longitudinal bar at the wall-foundation interface when the bar first yields at the interface, using the empirical relationship proposed by Zhao and Sritharan (2007). Afterwards, this cumulative slip/extension is divided by the yield strain of reinforcing steel, assuming a constant tensile strain distribution (both pre-yield and post-yield) on the reinforcing steel bar along the strain penetration depth, as described by Alvarez et al. (2020). Analysis results obtained using the updated model for the wall base rotations (measured along the bottom 0.6 m height of the wall W1– denoted as W11L in Fig. 32) reveal that consideration of strain penetration effects using this macroscopic modeling approach improves the model post-dictions for the wall base rotations, especially during the 50% amplitude excitation (Fig. 32a). However, wall base rotations measured during the 100% amplitude excitation are still moderately underestimated (Fig. 32b). This updated model configuration was used for presenting the analysis results shown in Fig. 32 only. Although not shown here for brevity, global response predictions obtained using the updated model did not significantly deviate from those obtained using the original model (shown in Figs. 25, 26, 27, 28 and 29), which did not consider strain penetrations effects on the walls.

Model predictions for wall shear distortions (average shear strains) are also compared with shear distortion measurements taken along the upper 2.2 m (W11U) of the first story height. The experimental shear distortions are calculated using the measurements of the diagonally-attached displacement sensors shown in Fig. 31, following the procedure described by Thomsen and Wallace (1995). The analytical shear distortions are calculated by adopting the same procedure, using the vertical and horizontal displacements at the model nodes that correspond to the sensor attachment points. Since the diagonal sensors attached along the bottom 0.6 m height of the wall (W11L) extended to the foundation and therefore straddled the wall-foundation interface crack, for a more consistent comparison, model predictions for shear distortions were compared with test measurements along the upper 2.2 m (W11U) of the first story height. Comparisons provided in Fig. 33 indicate that the model reasonably captures the experimentally-measured shear distortions in this wall region, during both the 50% amplitude and the 100% amplitude excitations, although the amplitudes of both the measured and predicted shear distortions are relatively small. It should be emphasized that the formulation of the LFSAFE model element does not require definition of a shear stiffness.

For evaluating the response simulations in terms of the local deformations developing in other structural components of the test building, model predictions for beam end rotations are compared with the rotations measured at both ends of a representative beam located at the fourth-floor level of the building (beam G7-2, Fig. 12a). The beam is oriented in the wall direction of the test building and frames into a rectangular wall at one end, and into a beam-column joint at the other end. Beam end rotation (i.e., relative rotation) measurements are obtained from the displacement sensors (LVDTs) installed longitudinally along the top and bottom of the beam, along a gauge length 0.6 m measured from the face of the wall or column. In the analysis results, relative rotations at beam ends are calculated as the difference in the rotation values obtained at two nodes of the beam-column model element, where the two nodes correspond to the two ends of the same gauge length. Comparison of measured and estimated beam end rotations under the 50% (Fig. 34a) and 100% (Fig. 34b) excitation levels show that the analysis model well-predicts the amplitudes and response histories of the relative rotations at both ends of beam, under both excitations, although the peak rotation amplitudes measured at the column connection of the beam (G7-2 N) are slightly overestimated during the 100% amplitude excitation.

As a final local deformation response comparison, model predictions are compared with rotations measured at the base of two first-story columns in the test building (columns C1 and C2, Fig. 12a). The column base rotations considered in the comparison are in the wall direction of the building. The experimentally-measured base rotations are obtained from

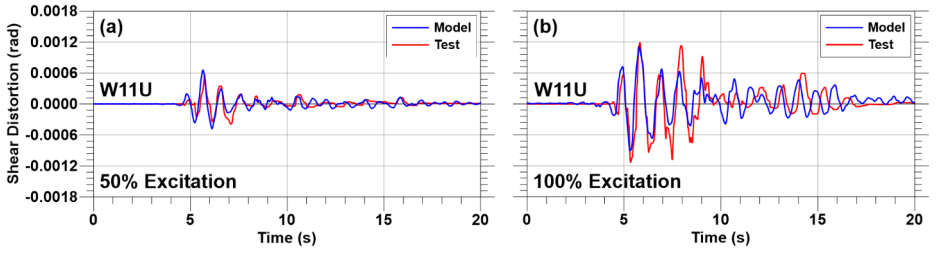

Fig. 33 Wall shear distortion time histories of the E-Defense test building under: (**a**) 50%, and (**b**) 100% excitation

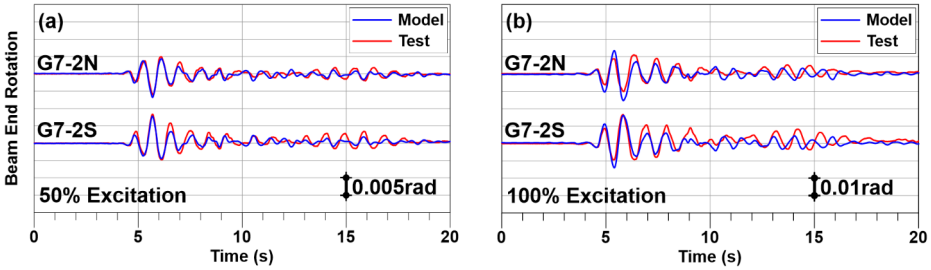

Fig. 34 Beam end rotation time histories of the E-Defense test building under: (**a**) 50%, and (**b**) 100% excitation

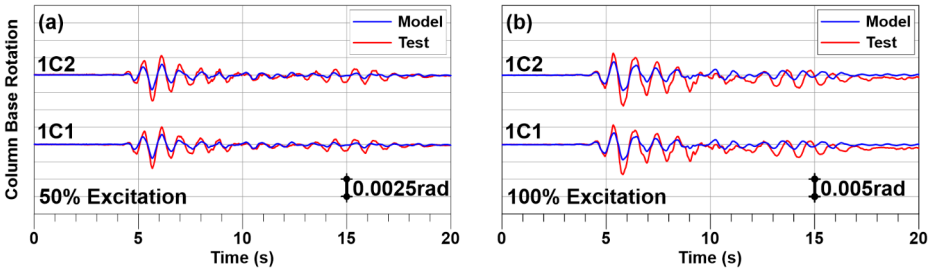

Fig. 35 Column base rotation time histories of the E-Defense test building under: (**a**) 50%, and (**b**) 100% excitation

vertical displacement sensors (LVDTs) attached to the column faces at one end, and to the top of the foundation at the other end, along a gauge length of 0.6 m. In the analysis model, since the beam-column model elements used for the columns incorporate fixed supports at the base, the analytical rotations are directly obtained from the rotations of the model element nodes that are located at a distance 0.6 m from the base. Response comparisons presented in Fig. 35a and b reveal that the model tends to underestimate the experimentally-measured base rotations on the columns, during both the 50% and 100% amplitude excitations. This discrepancy is in line with underestimation of the maximum drift ratios along the first story of the building (Fig. 26), and may be associated with strain penetration effects (i.e., slip/extension of longitudinal bars within the foundation) on the columns, since interface cracks were also observed at the base of the columns in the test building.

In the analytical response simulations for the E-Defense test building, yielding of longitudinal reinforcement observed at the base of the structural walls and columns, and at the beam end regions, are successfully simulated. Limited levels of cover concrete crushing observed at the base of the structural walls and the columns are also captured in the analysis results. Naturally, the experimentally-observed formation of continuous interface cracks at the wall-foundation and column-foundation interfaces is not represented in the response simulations, as the model is incapable of simulating formation of a continuous crack along multiple model elements. The most significant damage observed on the test building was shear damage on the beam-column joints, under displacements in the frame direction of the building, which does not reflect on the analysis results, since the nonlinear behavior of the beam-column joints is not considered in modeling. For this reason, all response compari-

sons that were presented in this paper are in the wall direction of the test building, along which noticeable beam-column joint damage was not observed during the experiment.

5 Future challenges

Worldwide, non-planar walls with increasingly complex non-rectangular cross-sectional geometries are being designed as core wall components in tall building construction. Some of these buildings also incorporate significant torsional irregularity. However, nonlinear modeling approaches recommended in performance-based design guidelines and typically implemented in industry-standard design applications fail to represent important response characteristics of such walls, including nonlinear shear/flexural/torsional interaction, nonlinear shear behavior, plane sections not remaining plane, torsional warping of the cross-section, and out-of-plane deformations in individual wall segments. Therefore, even in the immediate sense, improved nonlinear modeling approaches that can simulate such response characteristics of walls need to be made available to the engineering community, through widely-accessible computational platforms. The LFSAFE model presented in this paper was developed within the framework of the open-source analysis platform OpenSees, with such motivation. Of equal importance is the scarcity of dynamic test data available in the literature on walls, against which robust analytical models can be experimentally-validated. In addition to the shake table tests investigated (and cited) in this paper, further well-documented dynamic tests need to be conducted on large-scale and heavily-instrumented wall systems, with various geometric configurations and response characteristics, under various multi-directional excitations. Experimental data and observations from such dynamic test campaigns needs to be shared with the research/engineering community.

Although the LFSAFE model proposed in this paper (and further investigated in the companion paper by Tura et al. 2025) is presented as a powerful nonlinear analysis tool for RC walls, it inherently fails to simulate formation of a continuous crack at a wall-foundation interface, sliding shear deformations developing along the interface crack, and strain/yield penetration effects developing on the wall longitudinal reinforcement extending into the foundation. In reinforced concrete design standards, preventing sliding shear failure at the construction joints (i.e., cold joints) of walls is typically accounted for using very simple equations that define the shear-friction capacity at the joints, which do not prevent formation of an interface crack. Moreover, in performance-based design/assessment codes or guidelines, strain penetration effects are typically considered as a reduction in the linear elastic stiffness of the wall, together with an increase in wall deformation capacity (e.g., plastic rotation limit). As long as adequate shear friction capacity is provided at the joints and reduction in lateral stiffness due to strain penetration is accounted for in modeling, both sliding shear deformations and strain penetration effects are typically considered as secondary effects, which are not expected to notably impair the seismic performance of a wall, since both are expected to reduce the actual (physical) inelastic deformation demands developing in the walls at the material level (i.e., tensile strain demands on longitudinal reinforcement and shear distortion/strain demands on the wall). However, this may not always be the case. The rocking-type rotation induced due to strain penetration effects at a cracked wall-foundation interface may kinematically reduce the depth over which compressive stresses develop on the wall cross-section (i.e., reduce the neutral axial depth), and therefore increase the

compressive stress and strain demands on concrete at the compression end, possibly leading to a localized and premature crushing failure (i.e., toe crushing) at the base of the wall. Furthermore, sliding shear deformations developing along a cracked interface, although small in magnitude, may induce instabilities such as imperfect crack closure and kinking of the longitudinal reinforcing steel bars, and manifest in the form of premature concrete crushing and reinforcement buckling failures. Therefore, the influence of (*i*) cracking at wall-foundation interfaces, (*i*) sliding shear deformations developing along interface cracks, and (*iii*) strain penetration effects (rotations) accumulating at interface cracks on RC wall behavior and performance, need to be investigated in more detail, both experimentally and analytically.

6 Summary and conclusions

This paper presents a new layered-shell model element for RC walls–referred to as the Layered Fixed-Strut-Angle Finite Element (LFSAFE) model–developed within the framework of the computational platform OpenSees. The constitutive behavior and mechanical principles of the model element were described in this paper. Nonlinear dynamic response simulations obtained using the LFSAFE model were also presented, for: (*i*) a bi-directional shake table tests conducted on an isolated U-shaped wall specimen, and (*ii*) three-directional shake table tests conducted on a full-scale ten-story wall/frame building specimen. Contemplating the salient attributes of the LFSAFE model, and considering the dynamic response simulation results provided in this paper, the following conclusions are presented:

- The LFSAFE model element's three-dimensional formulation, with six degrees-of-freedom at each node, allows direct implementation in three-dimensional analysis models of entire structural systems. The drilling degrees of freedom in the model element allow direct connectivity with (and physical moment transfer to and from) connecting frame elements. The element's layered shell formulation considers nonlinear flexural behavior in the out-of-plane direction of a wall segment, permits a more detailed definition of the wall cross-section, and allows simulating non-uniform concrete crushing or reinforcement yielding across the wall thickness. Nonlinear response characteristics of the model element are based entirely on physical (behavioral) constitutive relationships, all of which were validated against test results at strain or local deformation levels.
- Simulation of shake table tests conducted on an isolated half-scale U-shaped wall specimen demonstrate the dynamic response prediction capabilities of the LFSAFE model in estimating the displacement, acceleration, and twist rotation response histories of non-planar walls exhibiting combined flexural-torsional behavior under bi-directional excitations.
- For the U-shaped wall specimen, accuracy of the local response predictions of the LFSAFE model for the average tensile strains developing at the base of the wall and the shear distortions developing on a wall flange were significantly improved when strain penetration effects on wall longitudinal reinforcement extending into the foundation were indirectly considered in modeling and the damping ratio assumed in analysis was recalibrated. The model failed to capture the concrete crushing and reinforcement out-of-plane buckling failure modes observed during the test at the flange-end boundary

regions of the wall, where the measured average compressive strains were drastically underestimated.

- Simulation of shake table tests conducted on a full-scale 10-story wall-frame building specimen tested under three-directional excitations have shown that the LFSAFE model was capable of providing reasonable predictions of the global response characteristics of the test building, including floor displacements, story drifts, and floor accelerations, as well as local deformation histories, including wall shear distortions and beam end rotations, although upper-floor accelerations, wall base rotations, and column base rotations in the building were moderately underestimated.
- Discrepancies in the model response predictions for the 10-story test building were found to be partially-related with neglecting, in the analysis model, the contribution of the floor slabs on the lateral stiffness of the test building, as well as the inability of the LFSAFE model to simulate formation of continuous wall-foundation interface cracks and the associated strain penetration effects on the walls. Modeling of the beams in the building using T-shaped fiber cross-sections improved the model predictions for the upper-floor accelerations, together with the associated base shear and the base overturning moment response histories of the building. Indirect consideration of strain penetration effects on modeling of the walls improved the wall base rotation estimations of the model.

Overall, the LFSAFE model is presented as very capable and versatile analysis tool for dynamic response simulation of non-planar walls and three-dimensional wall-frame systems. The companion paper presented in this special issue (Tura et al. 2025) focuses on detailed experimental validation of the LFSAFE model, against carefully-controlled quasi-static tests conducted on heavily-instrumented non-planar wall specimens subjected to multi-directional loading conditions. Further studies will focus on simulation of additional shake table tests conducted on isolated walls, wall systems, or wall-frame systems. The model formulation will be extended to incorporate robust constitutive modeling approaches for representing wall-foundation interface cracking and strain penetration effects on wall longitudinal reinforcement. The potential of utilizing the model not only for walls but also for RC slabs, will also be investigated. Upon further improvement and experimental validation, the LFSAFE model element will be made accessible to OpenSees users.

Acknowledgements For validation of the LFSAFE model, the authors have used data from the 2015 full-scale 10-story wall-frame building specimen tested under three-directional excitations at the E-Defense shake table facility, Hyogo Earthquake Engineering Research Center, National Research Institute for Earth Science and Disaster Resilience, Japan. The authors are grateful to the E-Defense team, who kindly invited them to join the project and shared the valuable experimental data with them, particularly to (in alphabetical order); H. Fukuyama, K. Fukuyama, T. Inoue, T. Kabeyasawa, T. Kabeyasawa, K. Kajiwara, J. Kang, T. Mukai, T. Nagae, E. Sato, H. Shiohara and Y. Tosauchi. The authors are also grateful to Dr. Ryan Hoult and Prof. João Pacheco de Almeida from Université Catholique de Louvain, for sharing very valuable experimental data from the 2024 shake table test conducted on the U-shaped wall specimen UWS1 at the National Laboratory for Civil Engineering (LNEC), Portugal.

Author contributions All readers read and approved the final manuscript.

Funding Open access funding provided by the Scientific and Technological Research Council of Türkiye (TÜBİTAK).
The authors declare that no funds, grants, or other support were received during the preparation of this manuscript.

Data availability The datasets generated during and/or analyzed during the current study are available from the corresponding author upon reasonable request.

Declarations

Conflict of interest The authors have no relevant financial or non-financial interests to disclose.

Open Access This article is licensed under a Creative Commons Attribution 4.0 International License, which permits use, sharing, adaptation, distribution and reproduction in any medium or format, as long as you give appropriate credit to the original author(s) and the source, provide a link to the Creative Commons licence, and indicate if changes were made. The images or other third party material in this article are included in the article's Creative Commons licence, unless indicated otherwise in a credit line to the material. If material is not included in the article's Creative Commons licence and your intended use is not permitted by statutory regulation or exceeds the permitted use, you will need to obtain permission directly from the copyright holder. To view a copy of this licence, visit http://creativecommons.org/licenses/by/4.0/.

References

Ahmed KA, Lowes LN, Lehman DE (2023) Investigation of the behavior of slender reinforced concrete walls with complex configurations using nonlinear finite element analysis. Resilient Cities Struct 2(1):120–142

Almeida JPd, Hoult R, Bertholet A, Candeias P, Carvalho A, Correia AA, Cumunel G, Doneux C, Han Y, Isakovic T, Janevski A, Lo Feudo S, Mihaylov B, Orgnoni A, Payen B, Palermo D, Pinho R, Ribeiro F, Simar A, Sousa ML (2024) Shake-table testing of two U-shaped RC walls: overview of the project ERIES-ALL4wALL. Procs. of 18th World Conference on Earthquake Engineering, Milan, Italy

Alvarez R, Restrepo JI, Panagiotou M (2020) RC wall plastic hinge out-of-plane buckling: analysis using the nonlinear beam-truss model. J Struct Eng 146(12):04020274

American Society of Civil Engineers (2017) Seismic evaluation and retrofit of existing buildings. ASCE/SEI 41–17

American Society of Civil Engineers (2023) Seismic evaluation and retrofit of existing buildings. ASCE/SEI 41–23

ANSYS Inc (2024) LS-DYNA theory manual. ANSYS Inc. Livermore, California

Architectural Institute of Japan (2010) AIJ Standard for Structural Calculation of Steel Reinforced Concrete Structures (in Japanese)

Batoz JL, Tahar M (1982) Evaluation of a new quadrilateral thin plate bending element. Int J Numer Methods Eng 18:1655–1677

Behrouzi AA, Mock AW, Lehman DE, Lowes LN, Kuchma DA (2020) Impact of bi-directional loading on the seismic performance of C-shaped piers of core walls. Eng Struct 225:111289

Bekaroglu EH (2019) Modeling of reinforced concrete membrane behavior considering shear stress transfer across cracks. M.S. Thesis, Boğaziçi University

Belarbi A, Hsu TTC (1994) Constitutive laws of concrete in tension and reinforcing bars stiffened by concrete. ACI Struct J 91:465–474

Bentley Systems (2024) ADINA Finite Element Analysis Software

Beyer K, Dazio A, Priestley MJN (2008a) Quasi-static Cyclic tests of two U-Shaped reinforced concrete walls. J Earthquake Eng 12(7):1023–1053

Beyer K, Dazio A, Priestley MJN (2008b) Inelastic wide-column models for U-shaped reinforced concrete walls. J Earthquake Eng 12(S1):1–33

Bilgin N, Gullu MF, Kolozvari K, Orakcal K (2021) Behavior and modeling of reinforced concrete walls, 9th Turkish Conference on Earthquake Engineering. Istanbul, Türkiye

Carrillo J, Alcocer SM (2012) Seismic performance of concrete walls for housing subjected to shaking table excitations. Eng Struct 41:98–107

Carrillo J, Alcocer SM (2013) Experimental investigation on dynamic and quasi-static behavior of low-rise reinforced concrete walls. Earthq Eng Struct Dynamics 42(5):635–652

Chang GA, Mander JB (1994) Seismic energy-based fatigue damage analysis of bridge columns: part 1—evaluation of seismic capacity. NCEER Technical Report No. NCEER-94-0006. Buffalo, USA

Chen MC, Pantoli E, Wang X, Astroza R, Ebrahimian H, Hutchinson TC, Conte JP, Restrepo JI, Marin C, Walsh KD, Bachman RRE, Hoehler MS, Englekirk R, Faghihi M (2016) Full-scale structural and non-structural Building system performance during earthquakes: part I–specimen description, test protocol, and structural response. Earthq Spectra 32(2):737–770

Computers and Structures Inc (2023) Perform3D V9.0 Nonlinear Analysis and Performance Assessment for 3D Structures

Constantin R, Beyer K (2016) Behavior of U-shaped RC walls under quasi-static Cyclic diagonal loading. Eng Struct 106:36–52

Dashti F, Dhakal RP, Pampanin S (2017) Numerical modeling of rectangular reinforced concrete structural walls. J Struct Eng 143(6):04017031

Dhakal RP, Maekawa K (2002a) Path-dependent Cyclic stress-strain relationship of reinforcing bar including buckling. Eng Struct 24(11):1383–1396

Dhakal RP, Maekawa K (2002b) Reinforcement stability and fracture of cover concrete in reinforced concrete members. J Struct Eng 128(10):1253–1262

DIANA FEA BV (2022) DIANA finite element analysis user manual release 10.5. Delft, The Netherlands

DIANA FEA BV (2024) DIANA finite element analysis user manual release 10.9. Delft, The Netherlands

Ebrahimian H, Astroza R, Conte JP, Hutchinson TC (2018) Pretest nonlinear finite-element modeling and response simulation of a full-scale 5-story reinforced concrete Building tested on the NEES-UCSD shake table. J Struct Eng 144(3):04018009

Feng DC, Ren XD, Li J (2018) Cyclic behavior modeling of reinforced concrete shear walls based on softened damage-plasticity model. Eng Struct 166:363–375

Filippou FC, Popov EP, Bertero VV (1983) Effects of bond deterioration on hysteretic behavior of reinforced concrete joints. Report EERC 83–19, Earthquake Engineering Research Center, University of California, Berkeley

Ghosh S, Dashti F, Nagae T, Uta H (2024) Numerical simulation of the 2010 4-story reinforced concrete structure tested on the E-defense shake table. Eng Struct 306:117769

Grange S, Kotronis P, Mazars J (2009) Numerical modelling of the seismic behavior of a 7-story building: NEES benchmark. Mater Struct 42:1433–1442

Gullu MF (2019) Nonlinear finite element modeling of RC structural walls. Dissertation, Boğaziçi University

Gullu MF, Orakcal K (2021) Nonlinear finite element modeling of reinforced concrete walls with varying aspect ratios. J Earthquake Eng 25(10):2033–2064

Gullu MF, Orakcal K, Kolozvari K (2018a) Nonlinear finite element modeling of squat walls with shear-dominant behavior. Proc. of 11th National Conference in Earthquake Engineering, Los Angeles, California, USA

Gullu MF, Orakcal K, Kolozvari K (2018b) Finite element modeling of low-rise shear-controlled structural walls. Proc. of 16th European Conference on Earthquake Engineering, Thessaloniki, Greece

Gullu MF, Orakcal K, Kolozvari K (2019) The fixed-strut-angle finite element (FSAFE) model for reinforced concrete structural walls. Bull Earthq Eng 17:6463–6489

He XG, Kwan AKH (2001) Modeling dowel action of reinforcement bars for finite element analysis of concrete structures. Comput Struct 79:595–604

He J, Chen J, Ren X, Li J (2020) A shake table test study of reinforced concrete shear wall model structures exhibiting strong non-linear behaviors. Eng Struct 212:110481

Hoult R, Almeida JP (2024) Modified compression field theory and disturbed stress field model on the simulation of the global and local behavior of non-planar reinforced concrete walls under Cyclic and dynamic loading. Bull Earthq Eng. https://doi.org/10.1007/s10518-024-01982-1

Hoult R, Almeida JPd, Correia AA (2024) Overview and blind prediction from shake table tests of a large-scale RC U-shaped core wall. Procs. of 18th World Conference on Earthquake Engineering, Milan, Italy

Hoult R, Beyer K (2021) RC U-shaped walls subjected to in-plane, diagonal, and torsional loading: new experimental findings. Eng Struct 233:111873

Hoult R, Bertholet A, Almeida JP (2022) Vertical displacement and strain measurements of RC walls using fiber-optic sensors and conventional instrumentation. Procs. of 8th Asia Conference on Earthquake Engineering, Taipei, Taiwan

Hoult R, Doneux C, Almeida JP (2023a) Tests on reinforced concrete U-shaped walls subjected to torsion and flexure. Earthq Spectra 39(4):2685–2710

Hoult R, Correia AA, Almeida JP (2023b) Beam-truss models to simulate the axial-flexural-torsional performance of RC U-shaped wall buildings. CivilEng 4(1):292–310

Isakovic T, Tabata K, Wallace J, Polese M (2023) International joint research on the full-scale ten-story RC buildings tested at E-Defense shaking table. Bull Earthq Eng 21(15):6499–6510

Jung JW, Ha JG, Hahm D, Kim MK (2021) In-structure response evaluation of shear wall structure via shaking table tests. J Earthq Eng Soc Korea 25(3):129–135

Kajiwara K, Tosauchi Y, Sato E, Fukuyama K, Inoue T, Shiohara H, Kabeyasawa T, Nagae T, Fukuyama H, Kabeyasawa T, Mukai T (2017) 2015 Three-dimensional shaking table test of a 10-story reinforced concrete building on the E-Defense part 1: overview and specimen design of the base slip and base fixed tests. Procs. of 16th World Conference on Earthquake Engineering, Santiago, Chile

Kajiwara K, Tosauchi Y, Kang J, Fukuyama K, Sato E, Inoue T, Kabeyasawa T, Shiohara H, Nagae T, Kabeyasawa T, Fukuyama H, Mukai T (2021) Shaking-table tests of a full-scale ten-story reinforced concrete Building (FY2015). Phase I: Free-standing system with base sliding and uplifting. Eng Struct 233:111848

Kang J, Kajiwara K, Fukuyama K, Sato E, Inoue T, Kabeyasawa T, Shiohara H (2020) E-Defense test of a 10-story reinforced concrete building (FY2018) Proc. of 17th World Conference on Earthquake Engineering, Sendai, Japan

Kolozvari K, Arteta C, Fischinger M, Gavridou S, Hube M, Isakovic T, Lowes L, Orakcal K, Vasquez J, Wallace JW (2018) Comparative study on state-of-the-art macroscopic models for planar reinforced concrete walls. ACI Struct J 115:1637–1657

Kolozvari K, Biscombe L, Dashti F, Dhakal RP, Gogus A, Gullu MF, Henry RS, Massone LM, Orakcal K, Rojas F, Shegay A, Wallace J (2019) State-of-the-art in nonlinear finite element modeling of isolated planar reinforced concrete walls. Eng Struct 194:46–65

Kolozvari K, Kalbasi K, Orakcal K, Wallace J (2021) Three-dimensional model for nonlinear analysis of slender flanged reinforced concrete walls. Eng Struct 236:112105

Kolozvari K, Gullu MF, Orakcal K (2022) Finite element modeling of reinforced concrete walls under uni- and multi-directional loading using opensees. J Earthquake Eng 26(12):6524–6547

Li W, Li QN (2012) Seismic performance of L-shaped RC shear wall subjected to Cyclic loading. Struct Des Tall Special Build 21(12):855–866

Lu Y, Panagiotou M (2014) Three-dimensional Cyclic beam-truss model for nonplanar reinforced concrete walls. J Struct Eng 140(3):04013071

Lu X, Xie L, Guan H, Huang Y, Lu X (2015) A shear wall element for nonlinear seismic analysis of super-tall buildings with opensees. Finite Elem Anal Des 98:14–25

Lu Y, Panagiotou M, Koutromanos I (2016) Three-dimensional beam-truss model for reinforced concrete walls and slabs–part 1: modeling approach, validation, and parametric study for individual reinforced concrete walls. Earthq Eng Struct Dynamics 45(9):1495–1513

Lu X, Tian Y, Cen S, Guan H, Xie L, Wang L (2017) A high-performance quadrilateral flat shell element for seismic collapse simulation of tall buildings and its implementation in opensees. J Earthquake Eng 22(9):1662–1682

Lu X, Tian Y, Sun C, Zhang S (2019) Development and application of a high-performance triangular shell element and an explicit algorithm in opensees for strongly nonlinear analysis. Comput Model Eng Sci 120(3):561–582

Mander JB, Priestley MJN, Park R (1988) Theoretical stress-strain model for confined concrete. ASCE J Struct Eng 114(8):1804–1826

Mansour MY, Hsu TC (2005) Behavior of reinforced concrete elements under Cyclic shear. ASCE J Struct Eng 131(1):54–65

Mansour M, Hsu TTC, Lee JY (2002) Pinching effect in hysteretic loops of R/C shear elements. ACI Special Publication 205:293–322

Martinelli P, Filippou FC (2009) Simulation of the shaking table test of a seven-story shear wall Building. Earthq Eng Struct Dynamics 38(5):587–607

McKenna F, Fenves GL, Scott MH (2000) Open system for earthquake engineering simulation. University of California, Berkeley, California ⟨http://opensees.berkeley.edu⟩

Menegotto M, Pinto E (1973) Method of analysis for cyclically loaded reinforced concrete plane frames including changes in geometry and nonelastic behavior of elements under combined normal force and bending. Procs. of IABSE Symposium on Resistance and Ultimate Deformability of Structures Acted on by Well-defined Repeated Loads. Lisbon, Portugal

Ministry of Land Infrastructure, Transport, and Tourism of Japan (2007) Technological Standard Related to Structures of Buildings (in Japanese)

MSC Software (2007) Marc 2007 r1 user's guide. MSC Software, Santa Ana, California

Nagae T, Tahara K, Matsumori T, Shiohara H, Kabeyasawa T, Kono S, Nishiyama M, Wallace J, Ghannoum W, Moehle J, Sause R, Keller W, Tuna Z (2011) Design and instrumentation of the 2010 E-Defense four-story reinforced concrete and post-tensioned concrete buildings. PEER Rep No. 2011/104.Pacific Earthquake Engineering Research Center, University of California, Berkeley, CA.

Nagae T, Matsumori T, Shiohara H, Kabeyasawa T, Kono S, Nishiyama M, Moehle J, Wallace J, Sause R, Ghannoum W, US National Conference on Earthquake Engineering (2014) The 2010 E-defense shaking table test on four-story reinforced concrete and post-tensioned concrete buildings. In 10th: Frontiers of Earthquake Engineering, Earthquake Engineering Research Institute, Oakland, California

Orakcal K, Massone LM, Ulugtekin D (2019) A hysteretic constitutive model for reinforced concrete panel elements. Int J Concrete Struct Mater 13:1–23

Panagiotou M, Restrepo JI, Conte JP (2011) Shake-table test of a full-scale 7-story Building slice. Phase I: rectangular wall. J Struct Eng 137(6):691–704

Pantoli E, Chen MC, Wang X, Astroza R, Ebrahimian H, Hutchinson TC, Conte JP, Restrepo JI, Marin C, Walsh KD, Bachman RE, Hoehler MS, Englekirk R, Faghihi M (2016a) Full-scale structural and non-structural Building system performance during earthquakes: part II–NCS damage States. Earthq Spectra 32(2):771–794

Pantoli E, Chen MC, Hutchinson TC, Astroza R, Conte JP, Ebrahimian H, Restrepo JI, Wang X (2016b) Landmark data set from the Building nonstructural components and systems (BNCS) project. Earthq Spectra 32(2):1239–1259

Rahman MM, Nahar TT, Kim D, Park DW (2022) Numerical modeling and shake table test for seismic response evaluation of an auxiliary Building in NPP with reinforced concrete shear wall. Nucl Technol 208(9):1453–1470

Rojas F, Anderson JC, Massone LM (2016) A nonlinear quadrilateral layered membrane element with drilling degrees of freedom for the modeling of reinforced concrete walls. Eng Struct 124:521–538

Rojas F, Anderson JC, Massone LM (2019) A nonlinear quadrilateral thin flat layered shell element for the modeling of reinforced concrete wall structures. Bull Earthq Eng 17:6491–6513

Saatcioglu M, Razvi S (1992) Strength and ductility of confined concrete. ASCE J Struct Eng 118(6):1590–1607

Sato E, Tosauchi Y, Fukuyama K, Inoue T, Kajiwara K, Shiohara H, Kabeyasawa T, Nagae T, Fukuyama H, Kabeyasawa T, Mukai T (2017) 2015 three-dimensional shaking table test of a 10-story reinforced concrete building on the E-Defense part 2: specimen fabrication and construction, test procedure, and instrumentation program. Procs. of 16th World Conference on Earthquake Engineering, Santiago, Chile

Smith M (2014) ABAQUS/Standard User's Manual, Version 6.14-1. Dassault Systems Simulia Corporation

Stevens NJ, Uzumeri M, Collins MP (1991) Reinforced concrete subjected to reversed Cyclic shear—Experiments and constitutive model. ACI Struct J 88(2):135–146

Sun L, Xiaodong J, Zhuang Y, Kajiwara K, Kang JD, Nagae T (2023) Nonlinear modeling of the ten-story RC Building structure of 2015 E-Defense shaking table tests. Bull Earthq Eng 21:6647–6666

Tassios TP, Vintzēleou EN (1987) Concrete-to-concrete friction. J Struct Eng 113:832–849

Thermou GE, Papanikolaou VK, Kappos AJ (2014) Flexural behavior of reinforced concrete jacketed columns under reversed Cyclic loading. Eng Struct 76:270–282

Thomsen JH, Wallace JW (1995) Displacement-based design of reinforced concrete structural walls: an experimental investigation of walls with rectangular and T-shaped cross-sections. Report no CU/CEE-95-06. Department of Civil Engineering, Clarkson University

Thomsen JH, Wallace JW (2004) Displacement-based design of slender reinforced concrete structural walls-experimental verification. ASCE J Struct Eng 130(4):618–630

TNO DIANA BV (2011) DIANA finite element analysis user's manual release 9.4.4. Delft, The Netherlands

Tosauchi Y, Sato E, Fukuyama K, Inoue T, Kajiwara K, Shiohara H, Kabeyasawa T, Nagae T, Fukuyama H, Kabeyasawa T, Mukai T (2017) 2015 three-dimensional shaking table test of a 10-story reinforced concrete building on the E-Defense part 3: base slip and base fixed test results. Procs. of 16th World Conference on Earthquake Engineering, Santiago, Chile

Tura C, Orakcal K, Gullu MF, Ilki A (2025) A new layered shell model for reinforced concrete walls II: experimental validation against quasi-static tests. Bulletin of Earthquake Engineering. (under review)

Ulugtekin D MS(2010) Analytical modeling of reinforced concrete panel elements under reversed cyclic loadings, Thesis Boğaziçi University

Vecchio FJ (2000) Disturbed stress field model for reinforced concrete formulation. ASCE J Struct Eng 126(9):1070–1077

Vecchio FJ, Collins MP (1986) The modified compression-field theory for reinforced concrete elements subjected to shear. ACI Struct J 83(2):219–231

Vecchio FJ, Collins MP (1993) Compression response of cracked reinforced concrete. J Struct Eng 119:3590–3610

Vintzēleou EN, Tassios TP (1986) Mathematical models for dowel action under monotonic and cyclic conditions. Mag Concr Res 38(134):13–22

Vintzēleou E, Tassios, TP (1987) Behavior of dowels under cyclic deformations. ACI Struct J 84(1):18–30

Wang B, Wu MZ, Shi QX, Cai WZ (2023) Seismic performance of flanged RC walls under biaxial Cyclic loading. J Building Eng 64:105632

Waugh JD, Sritharan S (2010) Lessons learned from seismic analysis of a seven-story concrete test Building. J Earthquake Eng 14(3):448–469

Xiao J, Kwon OS, Bentz E, Jung JW, Kim M (2024) Effect of modeling assumptions on predicting seismic responses of a three-story reinforced concrete shear wall structure. Earthq Eng Struct Dynamics 53(1):414–431

Xu Y, Long YQ (1993) Quadrilateral membrane element with vertex rotational freedom from generalized compatible condition. Eng Mech 10(3):37–36 (in Chinese)
Zhang J, Zheng W, Cao W, Dong H (2019) Shaking table test of mid-rise concrete shear walls with a single layer of web reinforcement and inclined steel bars. Int J Civil Eng 17:1043–1055
Zhao J, Sritharan S (2007) Modeling of strain penetration effects in fiber-based analysis of reinforced concrete structures. ACI Struct J 104(2):133–141

Publisher's note Springer Nature remains neutral with regard to jurisdictional claims in published maps and institutional affiliations.

Authors and Affiliations

Cem Tura[1] · Kutay Orakcal[1] · M. Fethi Gullu[2] · Alper Ilki[3]

✉ Kutay Orakcal
kutay.orakcal@bogazici.edu.tr

Cem Tura
cem.tura@bogazici.edu.tr

M. Fethi Gullu
fethigullu@harran.edu.tr

Alper Ilki
ailki@itu.edu.tr

[1] Bogazici University, Istanbul, Türkiye

[2] Harran University, Sanliurfa, Türkiye

[3] Istanbul Technical University, Istanbul, Türkiye